Acta Materialia 174 (2019) 351–368

Contents lists available at ScienceDirect

Acta Materialia

journal homepage: www.elsevier.com/locate/actamat

Full length article

An atomic scale structural investigation of nanometre-sized η precipitates in the 7050 aluminium alloy

Tsai-Fu Chung [a], Yo-Lun Yang [b], Makoto Shiojiri [c], Chien-Nan Hsiao [d], Wei-Chih Li [e], Cheng-Si Tsao [a], Zhusheng Shi [b], Jianguo Lin [b], Jer-Ren Yang [a, *]

[a] Department of Materials Science and Engineering, National Taiwan University, Taipei, Taiwan
[b] Department of Mechanical Engineering, Imperial College London, London, SW7 2AZ, UK
[c] Kyoto Institute of Technology, Kyoto, 606-8585, Japan
[d] Taiwan Instrument Research Institute, Hsinchu, Taiwan
[e] E.A. Fischione Instruments, Inc., 9003 Corporate Circle, Export, PA, 15632, USA

ARTICLE INFO

Article history:
Received 17 March 2019
Received in revised form
17 May 2019
Accepted 19 May 2019
Available online 22 May 2019

Keywords:
Scanning-transmission-electron microscopy
Al-Zn-Mg-Cu (AA7050) aluminium alloy
η-type precipitates
Layer-by-layer growth
η_4' and η_{12} precipitates

ABSTRACT

Using high-angle-annular-dark-field (HAADF) scanning-transmission-electron microscopy (STEM), we have investigated η-precipitates in the Al-Zn-Mg-Cu (AA7050) aluminium alloy. The HAADF STEM images taken along the zone axes of $[10\bar{1}0]\eta$, $[1\bar{2}10]\eta$, and $[0001]\eta$ illustrated the projected atomic-scale configurations of η-$MgZn_2$ crystal. The precipitates developed in layer-by-layer growth, supplied with precursors such as Zn, Cu, and Mg, which were solute atoms segregated around the η/Al interfaces due to the higher lattice strain energy. Stacking faults and defect layers composed of flattened hexagons were frequently observed along the zone axes of $[1\bar{2}10]\eta$ and $[10\bar{1}0]\eta$, respectively, and their formation was elucidated, similarly taking into account the layer-by-layer growth. Occasional coalescence between two precipitates yielded a complicated boundary or a twin-like boundary. Based on the differences in orientation relationships between η-types and the Al matrix reported to date, two new types of η precipitates have been recognized and named η_4' and η_{12}.

1. Introduction

The lightweight AA7050 (Al-Zn-Mg-Cu) aluminium alloy possesses high strength owing to precipitate hardening [1]. The precipitation sequence for such aluminium alloys has been reported [1–17] as follows: super-saturated solid solution (SSSS) → GP zones (GP I and II [2–6]) → η' precipitates (4 variants [2,7–10]) → η precipitates (11 types, η_1-η_{11} [1,2,7,8,11–15]). Recently, Chung et al. [7], who identified GPII zones, η', and η_2 precipitates in AA7050 aluminium alloy by high-resolution transmission electron microscopy (HRTEM), have elucidated the transition mechanisms of GPII zone → η' precipitate and η' precipitate → η_2 precipitate. Bendo et al. [11], Marioara et al. [18], and Xu et al. [19] have analyzed the stacking structures in the η_1 and η_2 types on the atomic scale by Cs-corrected high-angle annular-dark-field (HAADF) scanning-transmission electron microscopy (STEM). However, the structures and the growth mechanisms of η-type precipitates on the atomic scale have not yet been completely elucidated.

The η phase possesses the space group of $P6_3/mmc$, and its stoichiometric composition in the equilibrium state is normally approximate to that of $MgZn_2$, which is known as a hexagonal C14 Laves phase in the Al-Zn-Mg-Cu aluminium alloys [1,2,7,11,12,14,16]. Generally, Laves phases exist in three fundamental structures: hexagonal C14, cubic C15 and dihexagonal C36 structures [20,21]. In these structures, they follow the variation of stacking sequences constituted by the A, B, and C and the A', B', and C' types of atomic arrays [22–26]. These 6 types, possessing variable four-layered structural units with the intervening layers of solute atoms along the thickness direction [22–26], were first proposed by Komura [22]. In terms of the stacking sequences, the C14 structure has AB' stacking; the C15, ABC stacking; and the C36, AB'A'C stacking. The atomic configurations of these three structures are suggested to be the Kagome net, based on the triangle, rhombohedral and hexagonal polytypes [20–24,27,28]. It is presumable that the changes in those 6 stacking sequences would be associated with the formation of different atomic configurations of η in the Al-

* Corresponding author.
E-mail address: jryang@ntu.edu.tw (J.-R. Yang).

https://doi.org/10.1016/j.actamat.2019.05.041
1359-6454/

Zn-Mg-Cu aluminium alloys. The details are worth further investigation.

On the other hand, the group-theoretical point of view [29–33] has been employed to propose the characterization of the precipitate morphology and the determination of the number of precipitate variants with respect to the matrix. Initially, Buerger and Graef et al. [29,30] visualized the crystals as occurring in shapes that follow the symmetry of the crystallographic 32 point-groups under the matrix-free circumstance. Considering the solid state transformation, Kalonji and Cahn [31] and Boudeulle [32] illustrated that the precipitates forming from the matrix should be associated with the superimposed symmetry elements. The common point group between the matrix and the precipitate is also called the intersection point group [29–33]. From this resulting point-group, it can be extrapolated that the rotation or shifting of crystal interfaces will occur when precipitates grow from the matrix [31]. Moreover, the order of the intersection point group can be employed to deduce the number of equivalently-distributed variants of precipitates, i.e., the ratio of the order of matrix point group to that of the intersection point group [31–33]. Some investigations of steel alloys [34], magnesium alloys [35], and aluminium alloys [1,36] have provided examples to illustrate the morphologies of the precipitates and the number of variants equivalently distributed in the matrix.

Much attention has been paid to the observation of the plate-like morphology of η_2 in the Al-Zn-Mg-Cu aluminium alloys, because of its orientation relationship, which is almost identical to that of η' due to the in-situ transformation of η' → η_2 [7], as shown in Table 1. As just mentioned, it is an intriguing subject for the application of point-group symmetries to the morphologies of crystals grown from crystalline matrixes. Here, in the present work a case study for the precipitates η' (or η_2) in the aluminium matrix is demonstrated. The developed morphology and the number of equivalently-distributed variants of η' (or η_2) are analysed by the intersection point-group between η' (or η_2) and the Al matrix. The analysis procedure can be illustrated as follows. The η' (or η_2) has the $P6_3/mmc$ space group, which belongs to the 6/mmm point group. Given that the point group of the Al matrix is $m\bar{3}m$ with an order of 48, the symmetry elements of the intersection point-group can be deduced from the orientation relationship between η' (or η_2) and the Al matrix. The resulting intersection point-group is determined to be the $\bar{3}m$ point group, with an order of 12. The number of variants can be determined to be the ratio of the order of the matrix point group to that of the intersection point group [31–33]. Therefore, 4 equivalently-distributed variants (48/12 = 4) of η' (or η_2) precipitates can form in the Al matrix. The morphology of η' (or η_2) based on the resulting intersection point-group of $\bar{3}m$ is suggested to be a di-hexahedron shape [29,30] at the nucleation stage. During the growth of an η' (or η_2) precipitate, the lattice mismatches of the interfaces between precipitate and matrix should be taken into account. It is appropriate to conclude that the resulting plate-like morphology of η' (or η_2) would be associated with the growth along the preferential directions with a low-strain energy on the hexagonal plane of this embryo of di-hexahedron crystal, so that the low strain-energy of the interface can be maintained [7]. It should be noted that although a number of investigations [1,35,36,38–40] have employed the above crystallographic method to determine the morphologies of precipitates [29,30], few of those works have connected them with the variable compositions of alloys, which lead to changes in lattice parameters to some extent (i.e., the lattice misfit). Therefore, the lower lattice misfit, dominating the lower interfacial energy during the growth of precipitates, should be considered a significant factor in the selected growth direction, for it leads to a different morphology [41,42]. The related viewpoint can be seen in previous investigations illuminating the growth morphology of precipitates [7,34,43,44]. By considering the lattice-mismatch factor, it can be found that the morphology of η' (or η_2) will eventually develop into the plate-like shape. For other types of η, their equivalent variants and morphologies are listed in Supplementary Table 1 in Supplementary Material I.

In low magnification TEM images, the plate-like or rod-like η precipitates are easily found in the Al matrix along the zone axes of $[001]_{Al}$, $[110]_{Al}$, and $[1\bar{1}2]_{Al}$ [2,3,7,8,11,12,18,19,49]. It has been reported [2,12,49] that along the $[001]_{Al}$ zone axis, a high number density of precipitates with the edge-on configurations of the $\{001\}_{Al}$ planes is recognized as the plate-like η_1-type precipitate. The orientation relationship of η_1 with respect to the Al matrix,

Table 1
The thirteen types of orientation relationships between η precipitates (η_1-η_{12} and η_4')[a] and Al matrix.

	Orientation relationship		Morphology	Ref.
η'[b]	$(0001)\eta'//(1\bar{1}\bar{1})_{Al}$	$[10\bar{1}0]\eta'//[110]_{Al}$	Hexagonal or rounded plate	[2,7,10–14,16,18,37,44-46]
η_1	$(10\bar{1}0)\eta_1//(001)_{Al}$	$[1\bar{2}10]\eta_1//[110]_{Al}$	Rod[d]	[2,7,8,11–13,15,16,44,47]
η_9	$(11\bar{2}0)\eta_9//(001)_{Al}$	$[1\bar{1}00]\eta_9//[110]_{Al}$	Hexagonal prism[d]	[7,11,12,44,48]
η_2	$(0001)\eta_2//(1\bar{1}\bar{1})_{Al}$	$[10\bar{1}0]\eta_2//[110]_{Al}$	Hexagonal or rounded plate	[2,7,11–14,16,18,44,45,47]
η_3	$(0001)\eta_3//(1\bar{1}\bar{1})_{Al}$	$[11\bar{2}0]\eta_3//[110]_{Al}$	Hexagonal or triangular plate	[2,7,11,12,16,44]
η_{10}	$(0001)\eta_{10}//(1\bar{1}\bar{1})_{Al}$	$[11\bar{2}0]\eta_{10}//[1\bar{3}\bar{4}]_{Al}$	Not indicated	[7,12,16,44]
η_{11}	$(0001)\eta_{11}//(110)_{Al}$	$[10\bar{1}0]\eta_{11}//[1\bar{1}\bar{1}]_{Al}$	Rod	[7,12,16]
η_4	$(0001)\eta_4//(110)_{Al}$	$[\bar{1}2\bar{1}0]\eta_4//[1\bar{1}\bar{1}]_{Al}$	Rod	[2,7,11–13,16,44,45]
η_4'[c]	$(0001)\eta_4'//(110)_{Al}$	$[1\bar{1}00]\eta_4'//[001]_{Al}$	Hexagonal plate or prism	Present work
η_5	$(\bar{1}2\bar{1}0)\eta_5//(1\bar{1}\bar{1})_{Al}$	$[30\bar{3}2]\eta_5//[110]_{Al}$	Rod	[2,7,11,12,16,45]
η_6	$(\bar{1}2\bar{1}0)\eta_6//(1\bar{1}\bar{1})_{Al}$	$[20\bar{2}1]\eta_6//[1\bar{1}2]_{Al}$	Rod	[2,7,11,12,16,45]
η_7	$(\bar{1}2\bar{1}0)\eta_7//(1\bar{1}\bar{1})_{Al}$	$[10\bar{1}4]\eta_7//[110]_{Al}$	Rod	[2,7,11,12,16,45]
η_8	$(\bar{1}2\bar{1}0)\eta_8//(1\bar{1}2)_{Al}$	$[0001]\eta_8//[31\bar{1}]_{Al}$	Rod	[2,7,11,12,16]
η_{12}[c]	$(0001)\eta_{12}//(1\bar{1}3)_{Al}$	$[11\bar{2}0]\eta_{12}//[110]_{Al}$	Plate	Present work

[a] The notations from η_1 to η_{11} are used by Degischer et al. [12]. The morphologies of η_1 to η_9, and η_{11} have been observed along the $<110>_{Al}$ zone axes. The morphology of η_{10} has not been identified by TEM, and the similar data were tabulated by Bendo et al. [11] and Chung et al. [7].
[b] The orientation relationship and morphology of η′ is listed for reference.
[c] The novel η_4' and η_{12}-type precipitates were first analyzed in this present work.
[d] The morphologies of η_1 and η_9 have been confirmed in this present work.

$(10\bar{1}0)\eta_1//(001)_{Al}$ and $[1\bar{2}10]\eta_1//[110]_{Al}$, can be analysed from the diffraction pattern [46,47]. Recently, Bendo et al. [11] have reported that HAADF STEM observation along the $[110]_{Al}$ zone axis apparently reveals the edge-on configuration of η_1 with an atomic zig-zag stacking structure in hexagonal $MgZn_2$, which was observed similarly in η_2 along the $[1\bar{1}2]_{Al}$ zone axis [3,18,19]. The zig-zag stacking structure possesses R units (the rhombohedral Zn-column units) and R^{-1} units (the relatively 180°-rotated rhombohedral Zn-column units). Particularly, in η_1, the structure consists of R/R^{-1} stacking order structures separated by the internal boundary, which is composed of flattened hexagonal stackings [11]. In works conducted by Singh et al. [50–53], Rosalie et al. [54,55], and Yang et al. [56] the flattened hexagonal arrays, which are adjacent to the rhombohedral atomic arrays of η_1, have frequently been observed, similar to those of Mg_4Zn_7 in the Mg-Zn(-Y) magnesium alloys. A previous work [52] provided comprehensive views of the transition structures in between Mg_4Zn_7-$MgZn_2$, and the atomic arrays of these two phases can thereby be distinguished. The flattened hexagonal unit in the Mg_4Zn_7 phase is regarded as an intrinsic defect, the zone of the deficient Zn solute atoms. For the perfect $MgZn_2$ phase, the stoichiometry does not allow this type of defect. In order to recognize the differences in the atomic structures of $MgZn_2$ and Mg_4Zn_7, it is vital to identify their corresponding unit cells. The unit cell of $MgZn_2$ contains two differently-oriented pairs of rhombohedral arrays, as shown in Supplementary Fig. 1a (Supplementary Material II). On the other hand, the unit cell of Mg_4Zn_7 contains six differently-oriented pairs of rhombohedral arrays, enveloped by two differently-oriented pairs of a flattened hexagonal array interweaved with a rhombohedral array, as shown in Supplementary Fig. 1b (Supplementary Material II) [52]. Whether the Mg_4Zn_7 phase occurs during the growth of η_1 in the Al-Zn-Mg-Cu aluminium alloys was not elucidated in the previous work [11].

It is known that the similar edge-on $(001)_{Al}$ configurations of η_1 and η_9, based on their orientation relationships (i.e., $(10\bar{1}0)\eta_1//(001)_{Al}$ and $[1\bar{2}10]\eta_1//[110]_{Al}$ for η_1, and $(11\bar{2}0)\eta_9//(001)_{Al}$ and $[1\bar{1}00]\eta_9//[110]_{Al}$ for η_9) would be hard to distinguish in low magnification TEM images along the $[110]_{Al}$ zone axis [7,11]. The relative rotation about 30° along $[0001]\eta_1$ leads to $[11\bar{2}0]\eta_9//[001]_{Al}$ [11], as portrayed in Fig. 1a, and results in different atomic arrangements on the projected facet of the $(110)_{Al}$ plane. However, owing to the very small number density of η_9, whether the atomic-scale structure of η_9 is really the same as that of η_1 has hardly been discussed in previous investigations [7,11,12,16,45,48]. This probing question of the atomic arrays of η_1 and η_9 will be reported in the present work.

In previous investigations [7,18,19,57], η_2 phases were observed in high-resolution (HR)-TEM images along the $[110]_{Al}$ zone axis [7,57], and in high-resolution (HR)-STEM images along the $[1\bar{1}2]_{Al}$ zone axis [18,19]. It was revealed that the η_2 with the edge-on configuration on the $(1\bar{1}\bar{1})_{Al}$ plane has $(0001)\eta_2$ spacing approximately equal to 4 times the $(1\bar{1}\bar{1})_{Al}$ spacing (i.e., $d(0001)\eta_2$ (~0.860 nm) ≅ $4d(1\bar{1}\bar{1})_{Al}$ ($\sim 4 \times 0.233 = 0.932$ nm) [57]. The HR-STEM investigations characterized that the η_2 phases have two kinds of intrinsic-stacking orders depending on the arrangements of the atomic columns. One is orthorhombic-like units connecting with rhombohedral-like units (O/R), named Type 1 order, and the other, rhombohedral-like units connecting with rhombohedral-like units (R/R) or the relatively rotated 180° rhombohedral-like units (R/R^{-1}), named Type 2 order [18,19]. It was suggested from the first principles calculation (using the Vienna ab initio simulation package, VASP) that the stable η_2 phases possess the Type 2 order owing to their better coherency with respect to the Al matrix and the lower formation enthalpy than those of the Type 1 order [18].

According to previous works [7,12], the η_3 type is presumed to differ in orientation from η_2 with respect to the Al matrix, where the orientation of η_3 is obtained by rotating η_2 about 30° along $[0001]\eta_2$, leading to $[11\bar{2}0]\eta_3//[110]_{Al}$ (i.e., $(0001)\eta_3//(1\bar{1}1)_{Al}$ and $[11\bar{2}0]\eta_3//[110]_{Al}$), as shown in Fig. 1b. Fig. 1c indicates that the differences of the orientation relationships of η_5, η_6, and η_7 with respect to η_4 are the relative rotations of ~11°, ~15°, and ~25° along the $[0001]\eta_4$ direction, respectively. Their atomic-scale structures have yet to be investigated. In addition, Table 1 also indicates the difference between η_4 and η_{11} possessing the relative rotation of 30° along the $[110]_{Al}$ direction, leading to $[10\bar{1}0]\eta_{11}//[11\bar{2}0]\eta_4//[110]_{Al}$.

On the basis of the orientation relationship and morphology of η_8 types [2,7,11,12,16], the rod-like hexagonal configuration is schematically shown in Fig. 1d. In addition, it has been suggested [7] that the η_8 phases serve as the nucleation sites of T phases formed at higher ageing temperature, for η_8 types and T phases possess nearly the same orientation relationships with respect to the aluminium matrix. In Figs. 1b and d, the supposed morphologies of the η_{10} and η_{11} types are also indicated based on their orientation relationships, as reported in previous references [12,16,45].

In the present paper, we describe the investigation of the atomic scale structures of η precipitates in ageing-treated AA7050 aluminium alloy by HAADF STEM. The atomic configurations, stacking faults or defects, orientation relationships with the Al matrix, morphologies, and growth mechanisms of the η-$MgZn_2$ crystal were elucidated from atomic images along the zone axes of $[10\bar{1}0]\eta$, $[1\bar{2}10]\eta$ and $[0001]\eta$ taken mainly using η_2-type precipitates, and from comparison of the shapes and atomic arrays of various η-type precipitates grown with different orientations. According to the differences in orientation relationships with respect to the Al matrix, two novel types of η-precipitates have been proposed and named η_4' and η_{12}.

2. Materials and methods

An AA7050 aluminium alloy (Al-6.25Zn-2.14Mg-2.23Cu-0.05Fe-0.03Si, wt.%) was used in this study. After solution treatment (at 475 °C for 1 h with water quenching), the samples were immediately treated with a three-step ageing treatment: ageing at 120 °C for 8 h, at 165 °C for 1 h, and at 174 °C for 8 h with an applied constant tensile stress of 162.5 MPa (hereafter referred to as creep-age forming samples, CAF samples) [58]. The pre-observed TEM specimens were prepared by cutting discs from the selected samples along their loading direction and thinned to 0.07 mm thickness before they were twin-jet electropolished in a mixture of 33% nitric acid and 67% methanol at − 20 °C with a working voltage of 10 V. Then, the oxidation layers and the sample thickness were assumedly reduced by an M1040 NanoMill TEM specimen preparation system (E.A. Fischione Instrument), and the hydrocarbon contamination was subsequently removed by an M1070 Nanoclean plasma cleaner (E.A. Fischione Instrument). Afterwards, the TEM specimens were observed with an FEI Titan Chemi-STEM equipped with a spherical aberration corrector (Cs-corrector), which achieves a ~0.1 nm probe size with a beam current of ~70 pA and a convergence semi-angle of ~19.8 mrad. HAADF STEM images were recorded with a collecting angle range of 7.9–42.8 mrad of a HAADF detector. It is guaranteed that artefacts in the images are not caused by this electron probe [59,60]. The structure models for various atomic configurations of η precipitates were constructed with VASP [61,62] using the structure data proposed by Marioara [18] and Wolverton et al. [63].

3. Results and discussion

Chung et al. [7], who investigated the precipitate sequence of GP

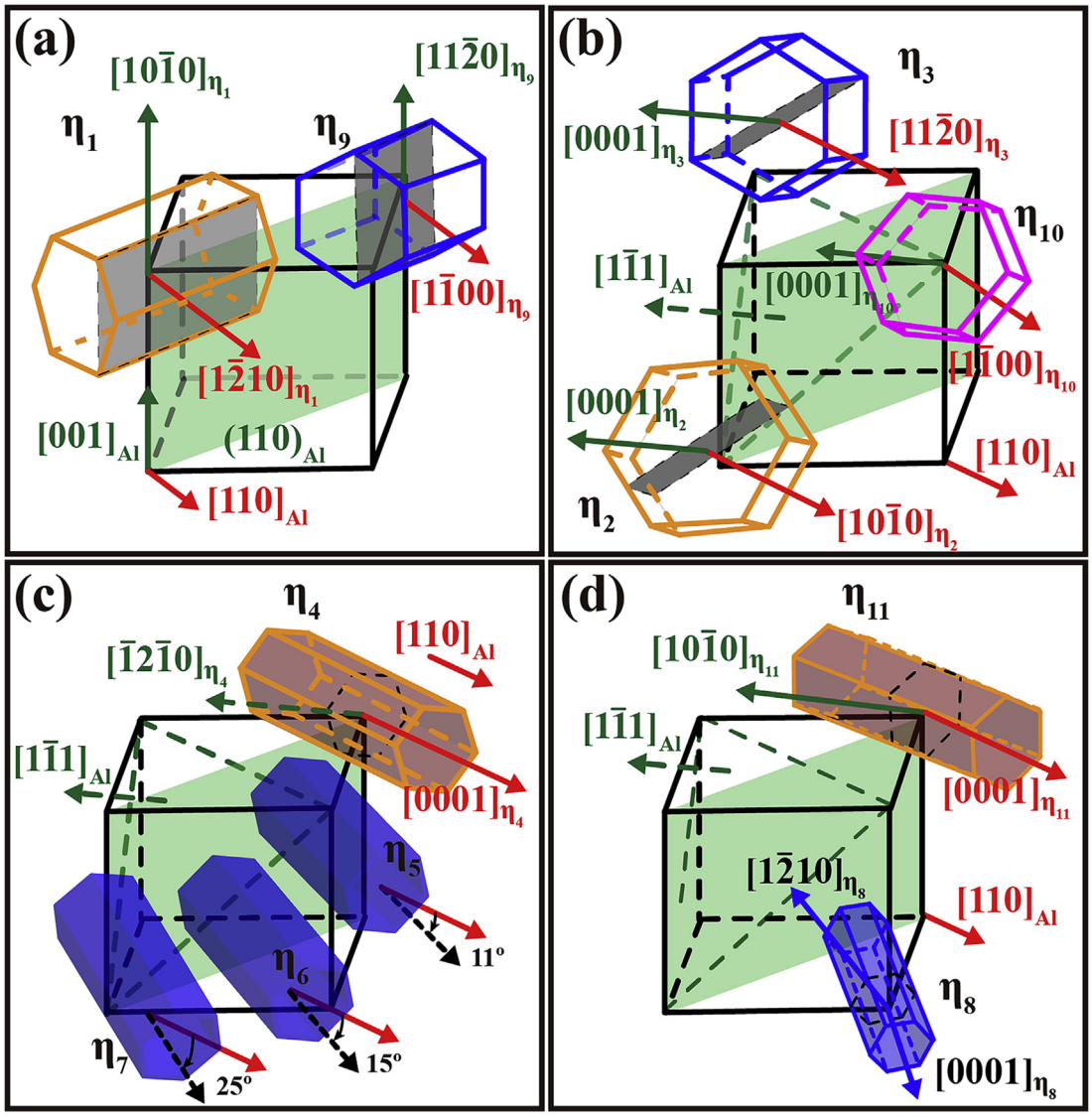

Fig. 1. The schematic diagram indicating the morphologies of different types of η precipitates and their orientation relationships with respect to the Al crystal. (a) η_1 and η_9; (b) η_2, η_3, and η_{10}; (c) η_4 and η_5–η_7; (d) η_8 and η_{11}.

zones → η' precipitates → η precipitates in the AA7050 aluminium alloy by TEM, reported that stable η_2 precipitates of larger size possess higher stability to prevent atomic-displacement or knock-on displacement caused by the electron beam during the observation, as compared to GP zones and η' precipitates. This provides a good opportunity to analyse the atomic structure of η precipitates by electron microscopy.

Fig. 2a shows an HR-HAADF STEM image of a precipitate, which was observed in the CAF film along the $[110]_{Al}$ zone axis. Fig. 2b shows an enlarged image of the area indicated by the frame in Fig. 2a. Fig. 2c shows the fast Fourier transform (FFT) diffractogram from the area in Fig. 2b and Fig. 2d is the simulated electron diffraction (ED) patterns for analysing Fig. 2c. From its orientation relation with respect to the Al matrix indicated in Fig. 2d and Table 1, the precipitate can be regarded as the η_2 type, which exhibits the edge-on configuration where the η_2 phase grew on the $(0001)\eta_2//(\bar{1}1\bar{1})_{Al}$ habit plane.

Generally, atomic-scale HAADF STEM images are formed by incoherent imaging with electrons elastically scattered by atoms [64,65]. Only the transverse composition of the relative displacement between the atoms in the atomic column illuminated by an electron beam is effective for HAADF STEM. The images are mainly formed by thermal-diffuse-scattering electrons and provide the atomic number (Z) contrast, approximately proportional to the squares of the atomic numbers of ^{12}Mg, ^{13}Al, ^{29}Cu or ^{30}Zn (the superscript is the Z) [66,67]. The intensity contrast is also proportional to the thickness of a material if the material is composed of the same elements. It should be noted that statistical displacements, such as differences in the position and size of atoms in alloys and the lattice distortion in deformed crystals, can cause electron diffuse scattering and contribute to HAADF STEM images. Furthermore, these displacements also influence the electron wave field in the crystal and thus HAADF STEM images [68]. The image in Fig. 2b closely resembles the simulated image for the structure of $MgZn_2$ [69] reported by Li et al. [70]. Therefore, it is appropriate to claim that Fig. 2b shows a Z-contrast image of the η_2-$MgZn_2$ precipitate exhibiting the regular variation of stacking layers, which we call sandwiched stacking structures. Thus, it can be proposed from the nominal composition of η_2 ($MgZn_2$) that the higher contrast layer (indicated by the blue arrowhead) is an array of columns mainly composed of Zn atoms and that the lower contrast layer (indicated by the green arrowhead) includes Mg-columns.

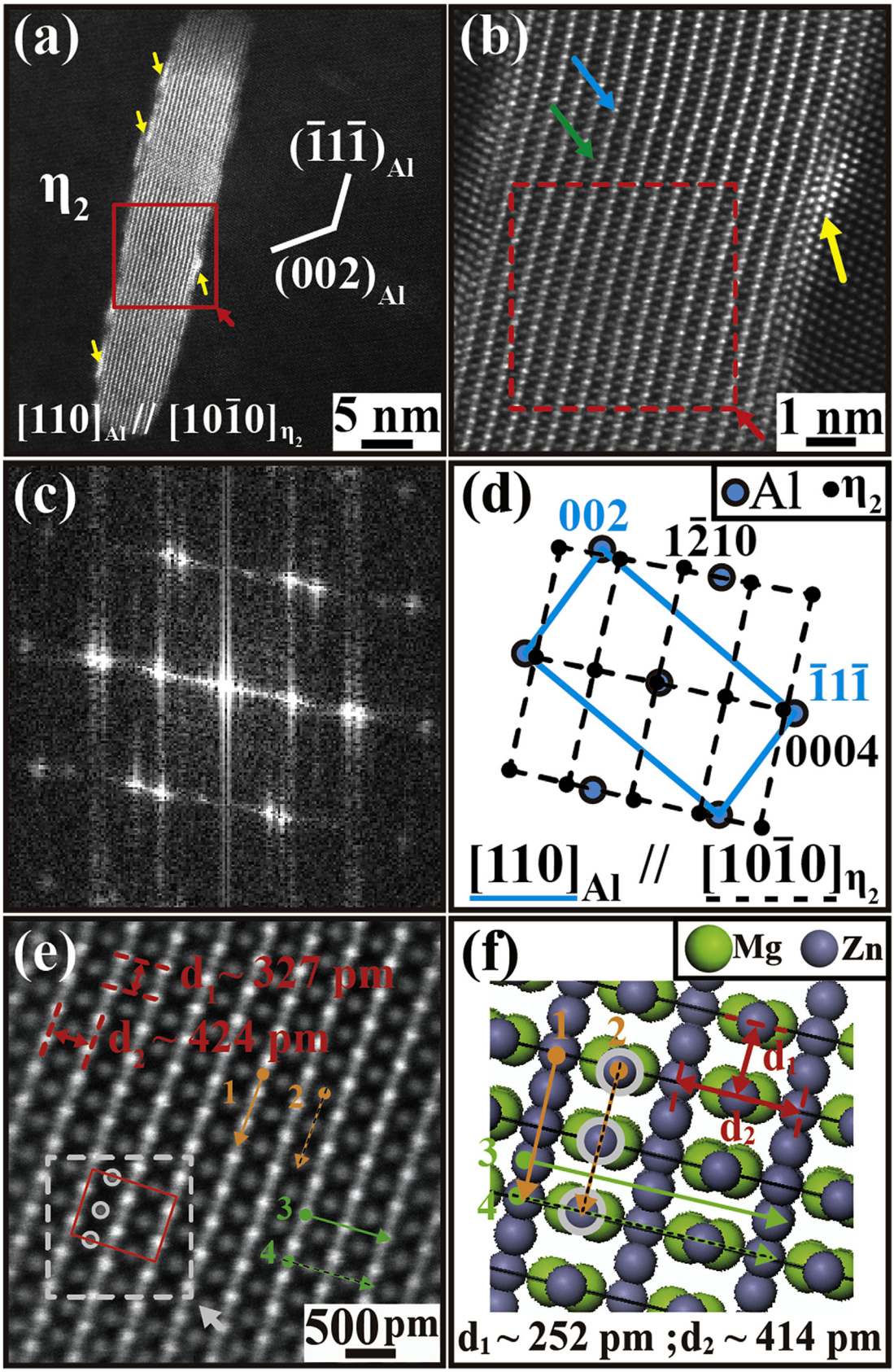

Fig. 2. An η_2 precipitate in ageing treated (CAF) AA7050 Al alloy. (a) A HAADF STEM image taken along the $[110]_{Al}//[10\bar{1}0]\eta_2$ zone axis showing the edge-on configuration of η_2 on the $(\bar{1}1\bar{1})_{Al}$ plane. (b) An enlarged image of the area indicated by the frame in (a). (c) The FFT diffractogram from the area of (b). (d) The simulation ED pattern. (e) An enlarged image of the area indicated by the red frame in (b). (f) The atomic structure of η_2-$MgZn_2$, pointing out the atomic configuration of the white dashed frame (e). (For interpretation of the references to colour in this figure legend, the reader is referred to the Web version of this article.)

Apparently, the HAADF STEM image in Fig. 2b is correlated to the chemical composition of the η_2-$MgZn_2$ phase and the Al matrix. The atomic column intensity along the $[110]_{Al}$ direction in the Al matrix was measured on eleven $(\bar{1}11)$ lattice fringes, indicated by Lines 1–11 in Supplementary Fig. 2a (Supplementary Material II). Supplementary Fig. 2b (Supplementary Material II) illustrates the intensity line profile along Line 1. Supplementary Fig. 2c (Supplementary Material II) shows the intensities of 100 atomic columns on Lines 1–11. The average intensity was estimated to be 1400 ± 106 counts. The error (standard deviation) of 106 counts is higher than an assumed statistical variability of 37 ($\sim\sqrt{1400}$) counts in the case of detecting a constant beam (with an averaged intensity of 1400 counts). It is presumed that the larger intensity fluctuation among atomic columns is caused by vacancies of Al atoms or small amounts of solved atoms, such as Mg, Zn or Cu remaining in the Al matrix, indicating Z contrast, since the thickness can be regarded to be uniform over such a small region.

Fig. 2e shows the enlarged image of the area indicated by the red frame in Fig. 2b. Fig. 2f indicates the calculated structure of η_2, which was drawn using the lattice parameters of η_2 obtained by VASP [63] and corresponds to the image of the area indicated by the white dashed frame in Fig. 2e. To understand the correlation between the real and calculated structures of η_2, the foci were specifically placed on the spacings between atomic layers and the intensity line profiles along different lattice fringes. Using the Al matrix lattice fringes (assuming $d(002)_{Al} = 0.202$ nm) for calibration as indicated in Figs. 2c and d, the distances between atomic-columns parallel and vertical to the $[\bar{1}11]_{Al}$ direction, d_1 and d_2, are referred to as $1/2\, d(1\bar{2}10)\eta_2$ and $1/2\, d(0001)\eta_2$), $d_1 \sim 327$ pm and $d_2 \sim 424$ pm, as shown in Fig. 2e. The calculated distances are $d_{1(VASP)} \sim 252$ pm and $d_{2(VASP)} \sim 414$ pm, as indicated in Fig. 2f. Hence, the lattice constants of the present η_2 crystal are a ~0.654 nm and c ~0.848 nm, while theoretical and experimental lattice constants of $MgZn_2$ have been reported as $a = 0.504$ nm and $c = 0.828$ nm by VASP calculation [63], and $a = 0.522$ nm and $c = 0.857$ nm by X-ray diffraction [69], respectively. In any case, the incompatible result of the lattice constants might be caused by the dynamic η_2-precipitate chemistry changes and the vacancy-atom interactions during the ageing treatment, as suggested by Ringer and Hono [1]. It can be seen as the fluctuation of the intensity among equivalent atomic columns (along Lines 1, 2, 3, and 4 indicated in Figs. 2e and f) in the HAADF STEM image, as indicated in Supplementary Fig. 3 (Supplementary Material II). These figures present the intensity line profiles along the lattice fringes indicated by Lines 1 and 2 in Figs. 2e and f. Line 1 is a $[10\bar{1}0]$ projection of atoms on the plane at $z = 1/4$ in the space group $P6_3/mmc$, where the atoms occupy three positions of Wyckoff notation (6h). Taking into account the structure of $MgZn_2$ [69], Supplementary Fig. 3a (Supplementary Material II) shows that Line 1 may be regarded as an array of ⋯ Zn, 2Zn, Zn, 2Zn, ⋯ in a thickness of 2 unit cells or a double $(10\bar{1}0)$ plane. Similarly, Line 2, which is a projection of atoms at $z = 0$, is an array of ⋯ Zn, Zn, ⋯, which occupies positions at one position of Wyckoff notation (2a). Supplementary Fig. 3b (Supplementary Material II) shows the intensity line profiles along the lattice fringes indicated by Lines 3 and 4 in Figs. 2e and f. Line 3 is a $[10\bar{1}0]$ projection of atoms on one $(1\bar{2}10)$ plane and must be an array of ⋯ 2Zn, 2Zn, 2Zn, ⋯. Line 4 is a $[10\bar{1}0]$ projection of atoms on another $(1\bar{2}10)$ plane and must be an array of ⋯ Zn, Mg, Zn, Mg, Zn, Mg, Zn, Mg, Zn, Mg, ⋯. A general survey of these intensity line profiles exhibits the Z contrast of $MgZn_2$ crystal. The intensity among equivalent atomic columns on Line 1 (and also Lines 2, 3, and 4), however, does not seem the same within statistical variability. The fluctuation of intensity exceeding the statistical variability may be ascribed to the difference in chemical composition among the atomic columns, which is caused by substitution of ^{13}Al, ^{29}Cu, ^{26}Fe, or ^{14}Si atoms or vacancies for Zn sites (and also Mg sites on Line 4).

An area near the η_2/Al interfaces, indicated by a solid yellow arrow in Fig. 2b, exhibits abnormally strong bright contrast. Presumably, the lattice mismatch between the η_2 and Al crystals would cause higher interfacial energy or higher lattice strain energy near the interface of η_2/Al, inducing the change of solute atom concentration, which is suggested to be a chemical effect or Suzuki effect for segregation to stacking faults [71]. Hence, the brighter contrast in the HAADF STEM image is ascribable to the segregated Zn and also Cu atoms in the Al lattices near the interface, as similarly reported in previous investigations [72–80] revealing the segregation of solute atoms nearby the precipitate/matrix interfaces in magnesium alloys [72–74] and aluminium alloys [75–80].

Bendo [11] and Marioara et al. [18] observed a similar R/R^{-1} stacking layer-structure, which contains the rhombohedral-like unit (R) connecting with another rhombohedral-like unit (R^{-1}) rotated 180° relative to R, in HR-STEM images of η_1 and η_2 precipitates along the $[110]_{Al}$ and $[1\bar{1}2]_{Al}$ zone axes, respectively. These precipitates exhibit the edge-on configurations on the interfaces with the Al matrix parallel to the $(1\bar{1}\bar{1})_{Al}$ plane and possess the stacking layers in the precipitates. The R/R^{-1} was presumed to be one kind of stacking structures that existed in all types of η [11]. We also observed η_2 precipitates with the uniform R/R^{-1} stacking layers in HAADF-STEM images of the CAF sample along the $[1\bar{1}2]_{Al}$ zone axis, as seen in Fig. 3.

The growth of η precipitates can be interpreted simply as follows. An η precipitate or $MgZn_2$ crystal grown via η' from GPII zones in the Al matrix [7] has a characteristic habit plane, indicated in Table 1. As mentioned above, a kind of chemical effect segregates solute atoms such as Zn, Cu, and Mg from the matrix and diffuses them into a region near the interface of the η/Al crystals, which is a habit surface of the $MgZn_2$ crystal. Once a crystal nucleus forms on the surface of the precipitated $MgZn_2$ crystal, it grows laterally on the surface, supplied by precursors of Zn and Mg from the nearby matrix, which is rich with solute atoms. The layer-by-layer growth occurs following the most stable stacking sequence of $R\, R^{-1}\, R\, R^{-1}\, R\, R^{-1}$ … as $MgZn_2$ crystal, consecutively. As is often the case with layer-by-layer growth, steps form along the edges of layers, as indicated by small white arrowheads in Fig. 3a. The crystal goes on growing laterally at the steps, supplied with precursors. This mechanism is common in the growth of single crystal thin films of semiconductor material by methods such as metal-organic chemical vapour deposition and atomic layer deposition [81].

Two spacings, d_1 and d_2, indicated in Fig. 3c, were measured, and the results were $d_1 \sim 0.451$ nm and $d_2 \sim 0.833$ nm, which correspond to the lattice constants a and c, respectively. Both precipitates shown in Figs. 2 and 3 were in the same sample and of the same η_2 type but had lattice constants different from each other and from the calculated ones shown in Fig. 3d. The chemical composition must differ slightly among precipitates even if they are of the same type of η grown in the same sample. Bendo et al. [11] reported an example of the disrupted-arrangement inside η_1 where the R/R^{-1} stacking layers were separated by internal boundaries composed of irregular atomic arrangements, and they assumed that the precipitate was in the early stages of growth. The Z-contrasts can also be seen clearly in an enlarged image in Fig. 3e and are easily understandable from the structure schematically shown in Fig. 3f, where 3Zn, 2Zn, and 3Zn indicate Zn columns with 3, 2, and 3 atoms in the rhomb unit-cell, respectively. However, Mg-columns along the long diagonal line are blurred, possibly due to disturbance from the Al matrix beneath the precipitate and the weak Z-contrast intensity of Mg atoms.

Figs. 4a and b show HAADF-STEM images of a different sort of η_2

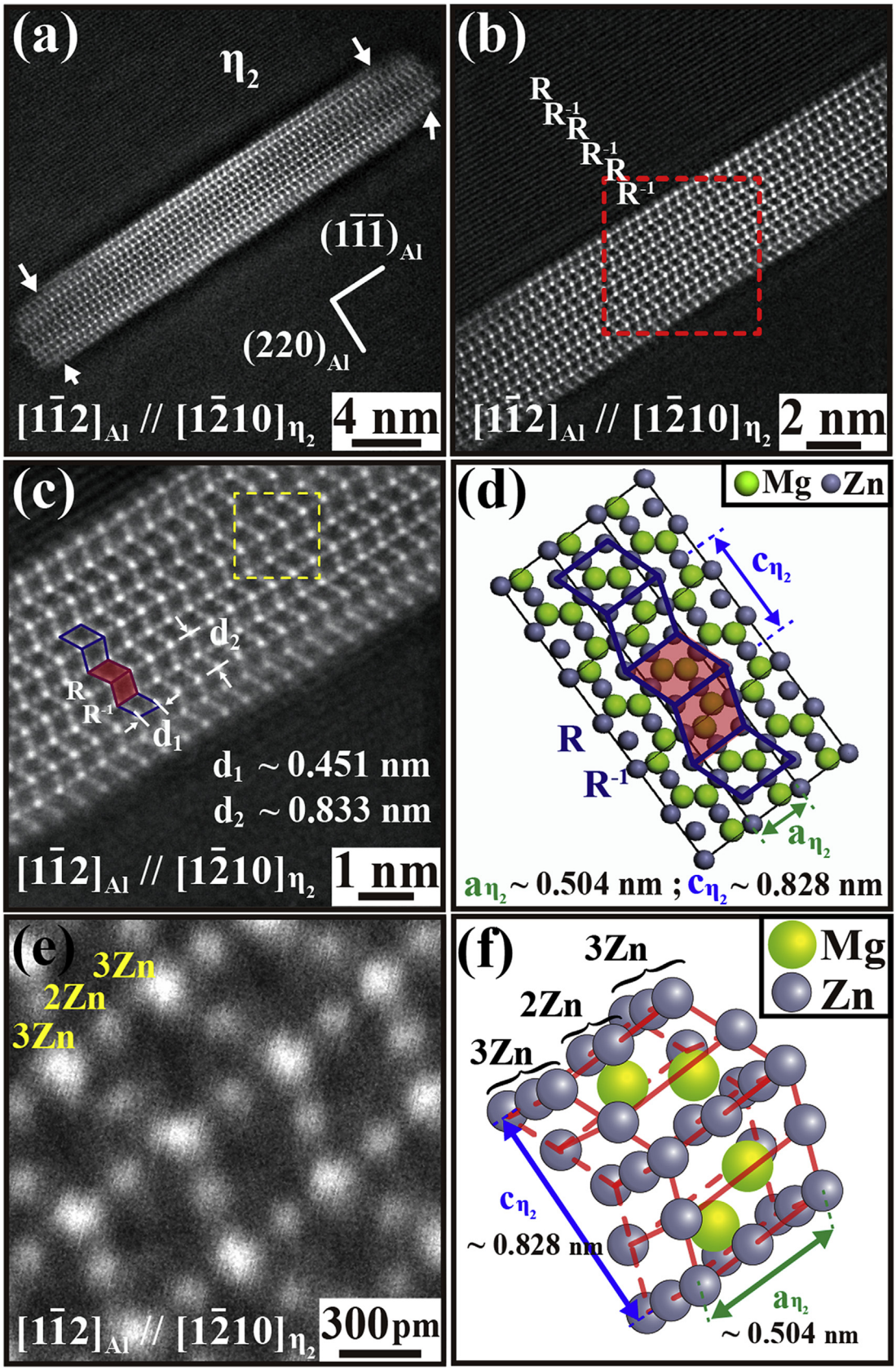

Fig. 3. Another η_2 precipitate in the CAF Al alloy. (a) A HAADF STEM image taken along $[1\bar{1}2]_{Al}//[1\bar{2}10]\eta_2$ zone axis showing its edge-on configuration on the $(1\bar{1}\bar{1})_{Al}$ plane. (b) An enlarged image of part of (a), exhibiting a sound ordering of R/R^{-1} in η_2. (c) The enlarged image of the area indicated by the frame in (b), indicating the measured lattice spacings, d_1 and d_2. (d) The structure of $MgZn_2$ projected along $[1\bar{1}2]_{Al}//[1\bar{2}10]\eta_2$, indicating calculated parameters, a and c. (e) An enlarge HAADF STEM image of rhomb (RR^{-1}) units. (f) A schema of a pair of RR^{-1} units, visualizing the atomic columns along the $[1\bar{2}10]\eta_2$ zone axis.

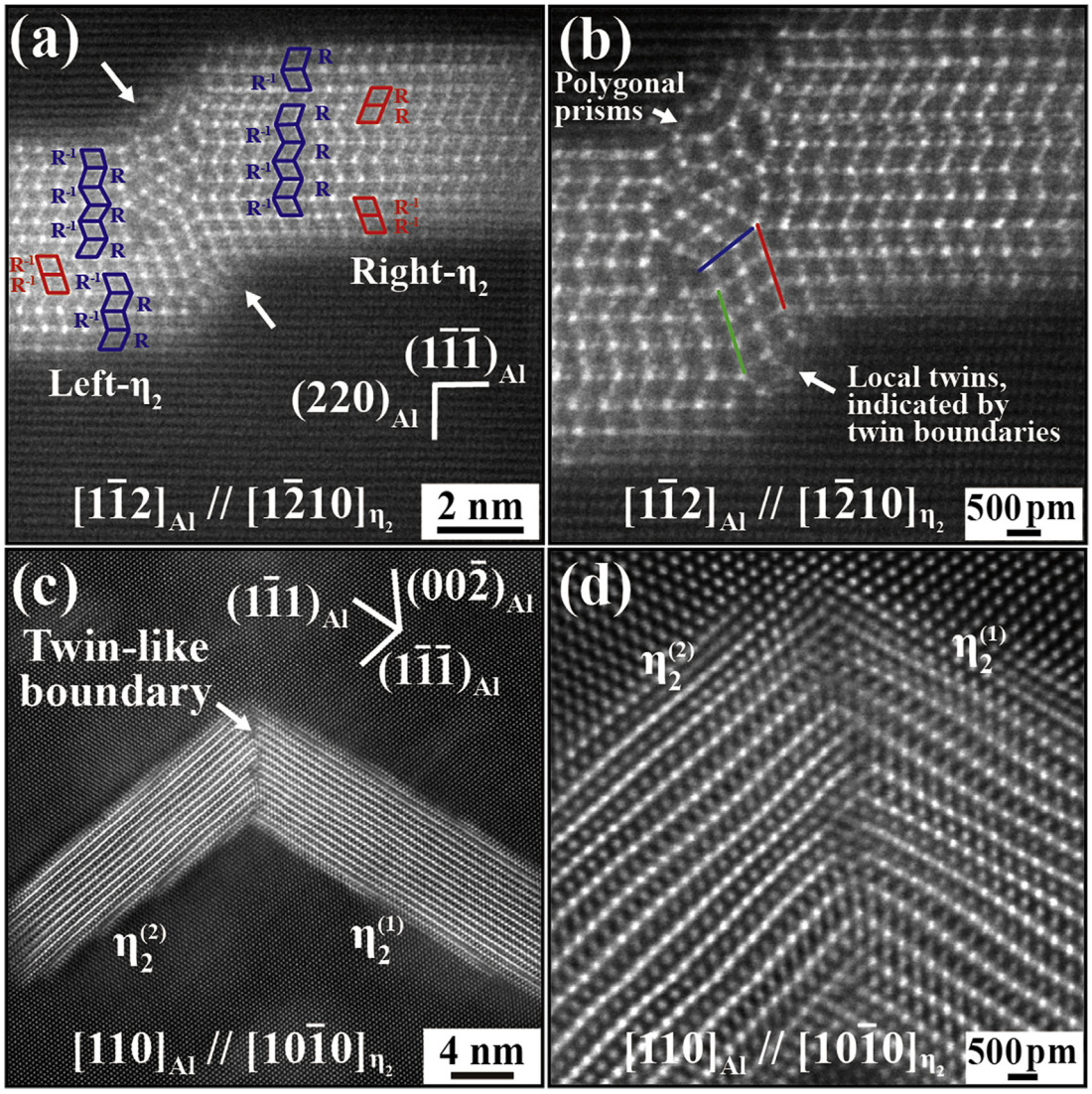

Fig. 4. Coalescence growth between η_2 crystals precipitated in the CAF Al alloy. (a) HAADF STEM image taken along the $[1\bar{1}2]_{Al}//[1\bar{2}10]\eta_2$ zone axis. Two crystals, left-η_2 and right-η_2, which precipitated on almost the same $(1\bar{1}\bar{1})_{Al}$ planes, coalesced. They had an R/R^{-1} stacking structure including stacking faults. (b) An enlarged image of the coalesced region in (a), revealing the complicated bonding boundary with local twinning and various defect structures. The twin boundaries are indicated by three coloured bars. (c) HAADF STEM image taken along the $[110]_{Al}//[10\bar{1}0]\eta_2$ zone axis. Two variants of η_2 precipitates, $\eta_2^{(1)}$ and $\eta_2^{(2)}$, which precipitated on different Al planes of $(1\bar{1}\bar{1})$ and $(1\bar{1}1)_{Al}$, respectively, coalesced and resulted in a twin-like structure. They exhibited a sandwiched structure. (d) An enlarged image of the coalesced region in (c), revealing the atomic arrays of the boundary.

precipitate grown on the $(1\bar{1}\bar{1})_{Al}$ plane, which were also observed along the $[1\bar{1}2]_{Al}$ zone axis in the Al matrix. The atomic configuration is composed of two parts: the left part, which comprises layers with $\cdots R^{-1}R \cdots /R^{-1}R^{-1}/ \cdots R^{-1}R \cdots$, and the right part, which comprises layers with $\cdots RR^{-1} \cdots /RR/ \cdots RR^{-1} \cdots /R^{-1}R^{-1}/ \cdots RR^{-1} \cdots$, as marked by blue and red frames in Fig. 4a. Both the left and the right parts have stacking faults such as RR or $R^{-1}R^{-1}$ against the proper ordering of $RR^{-1}RR^{-1}$. The existence of these stacking faults is not abnormal but rather common in η precipitates. These crystals grew layer-by-layer, separately. Once an embryo nucleated in an irregular stacking manner, the layer with this order would extend laterally over the surface layer, even if the formation of the stacking fault was unfavourable in energetics, because the ordering was controlled only by the secondary layer beneath the surface in the stacking structures. These stacking faults were of neither the Shockley-type nor the Frank-type because partial dislocations were never observed; rather, they were simple stacking faults caused by mis-stacking of the layer during the growth. It may be regarded as a result of the lateral growth and collision of two η_2 particles that precipitated on almost the same $(1\bar{1}\bar{1})_{Al}$ layers but with different stacking orders. Two particles encountered each other and then generated a complicated boundary (as indicated by arrows in Fig. 4a), which was composed of local twins and polygonal prisms, almost remaining atomic columns along $[1\bar{2}10]\eta_2//[1\bar{1}2]_{Al}$, as seen in Fig. 4b. Furthermore, Figs. 4c and d show HAADF STEM images of two variants of η_2-crystals with the sandwiched stackings, observed along the $[110]_{Al}$ zone axis. These two variants, indicated as $\eta_2^{(1)}$ and $\eta_2^{(2)}$, developed on two different Al planes of the $(1\bar{1}\bar{1})_{Al}$ and $(1\bar{1}1)_{Al}$ planes, respectively. They coalesced with a twin relation and the twin-like boundary was nearly parallel to the $(00\bar{2})_{Al}$ plane, as shown in Fig. 4d. Hence, we found that the specific boundaries which were formed by coalescence between two crystals precipitated on the same $(1\bar{1}\bar{1})_{Al}$ layers (as shown in Fig. 4a) or on different $\{1\bar{1}\bar{1}\}_{Al}$ layers (as shown in Fig. 4c).

Fig. 5a shows a HAADF-STEM image of a precipitate in the CAF Al alloy observed along the $[110]_{Al}$ zone axis. Fig. 5b shows an enlarged image of the area indicated by the frame in Fig. 5a, disclosing the atomic arrangement in detail. Its FFT diffractogram

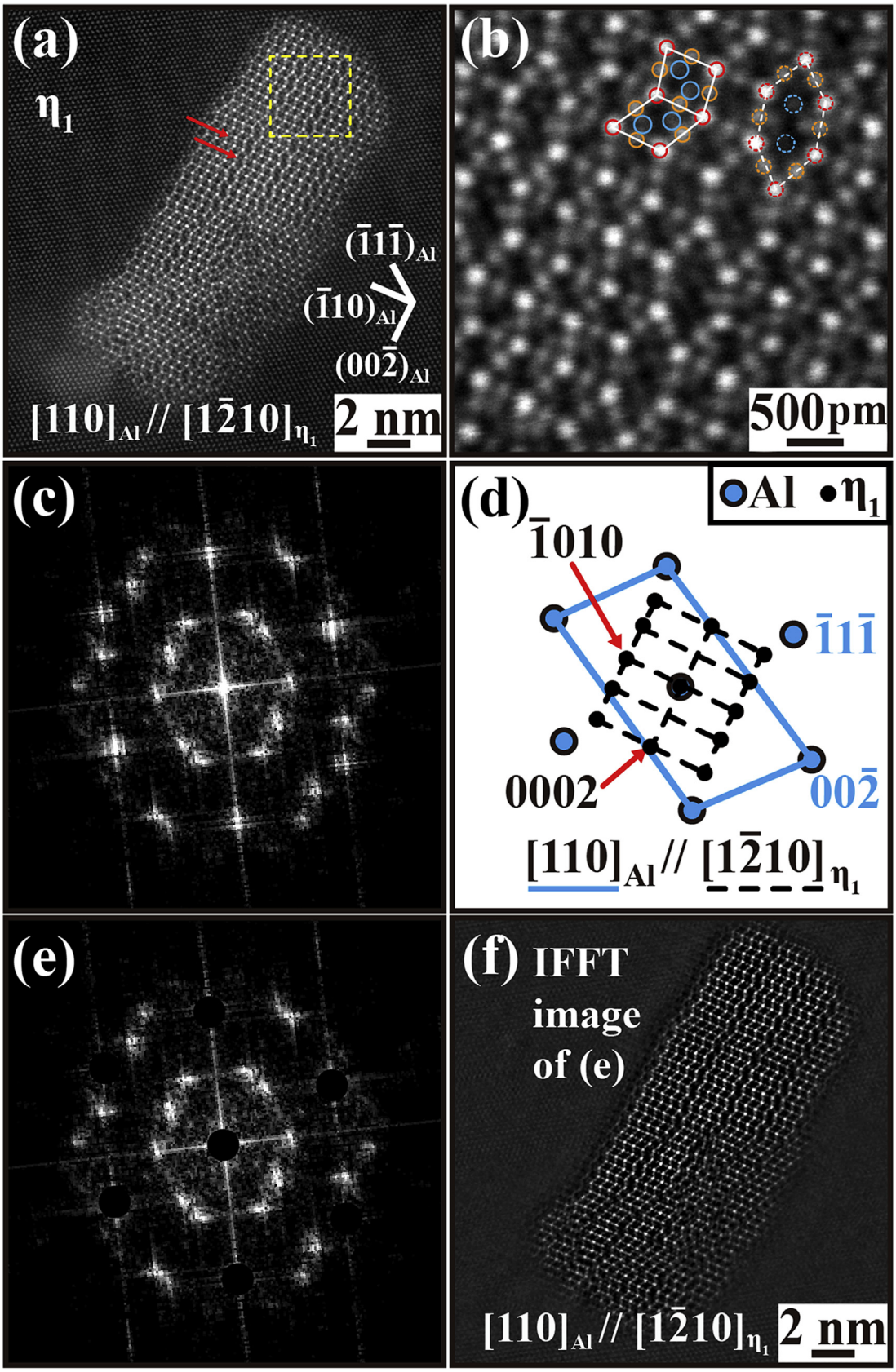

Fig. 5. An η_1 precipitate in the CAF Al alloy. (a) A HAADF-STEM image taken along the $[110]_{Al}//[1\bar{2}10]\eta_1$ zone axis showing its edge-on configuration on the $(00\bar{2})_{Al}$ plane. (b) An enlarged image of the area indicated by the yellow frame in (a), showing a couple of R/R^{-1} units in an $RR^{-1}RR^{-1}$ stacking layer and one of the flattened hexagons that form a defect layer between the $RR^{-1}RR^{-1}$ stacking layers. Red, orange, and blue circles indicate Zn, Zn/Mg, and Mg atomic columns, respectively. (c) FFT diffractogram from the whole area in (a). (d) Simulated ED pattern for the η_1 precipitate with the Al matrix, revealing the orientation relationship of $(10\bar{1}0)\eta_1//(001)_{Al}$ and $[1\bar{2}10]\eta_1//[110]_{Al}$. (e) The selected reflection spots only from η_1. (f) IFFT image reconstructed using (e), disclosing more clearly the structure of η_1, in particular irregular or flattened-hexagon layers and other defects in the RR^{-1} layers. (For interpretation of the references to colour in this figure legend, the reader is referred to the Web version of this article.)

shown in Fig. 5c confirmed this precipitate mainly to be an η_1 crystal with the orientation relationship of $(10\bar{1}0)\eta_1//(001)_{Al}$ and $[1\bar{2}10]\eta_1//[110]_{Al}$, considering the simulated ED patterns for η_1 and Al crystal shown in Fig. 5d. The main part of the precipitate comprised R/R^{-1} stacking layers. However, a layer composed of flattened hexagons, as projections of atomic columns, was observed between the regular R/R^{-1} stacking layers, as seen in the frame in Fig. 5a. This structure has been reported and analysed by Bendo et al. [11]. It may be noted that this η_1 precipitate grew laterally on the $(001)_{Al}$ plane, exhibiting the $(10\bar{1}0)\eta_1$ habit plane, while the η_2 precipitates grew laterally on the $(1\bar{1}\bar{1})_{Al}$ plane, exhibiting the $(0001)\eta_2$ habit plane. In other words, in the η_1 precipitate, layers of $\cdots RR^{-1}RR^{-1}\cdots$ grew laterally on the $(10\bar{1}0)\eta_1$ surface, successively, while in the η_2 precipitate, a layer of $\cdots RR\cdots$ and a layer of $\cdots R^{-1}R^{-1}\cdots$ grew laterally on the $(0001)\eta_2$ surface, alternately. The difference in growth between η_1 and η_2 precipitates may be ascribed to the difference in the initially-nucleated η_1 and η_2 layers on the $(001)_{Al}$ and $(1\bar{1}\bar{1})_{Al}$ planes, respectively, where Al planes are replaced by Zn/Mg atoms. As a result, the η_1 precipitates became rods, while the η_2 precipitates became plates, as shown in Table 1.

In Fig. 5a, the atomic arrays of $(0002)\eta_1//(\bar{1}10)_{Al}$ (as indicated by red arrows) do not pass through the fault layers composed of several flattened hexagonal arrays continuously connected with each other and neatly distributed on the $(00\bar{2})_{Al}$ plane; rather, they are suddenly interrupted by a single rhombohedral array in the layer. The stronger Zn fringes in Z contrast change to weaker Zn fringes. This can be clearly seen in Fig. 5f, which is the inverse FFT image reconstructed using only diffraction spots from η_1 (Fig. 5e) in the FFT diffractogram of the image in Fig. 5a. That is, the fringes of Zn atoms in Wyckoff position 6(h) changed to the fringes of Zn atoms in position 2(a) [69]. Therefore, the stacking fault layer can be regarded as a kind of antiphase boundary [11], which is clearly different from the typical structure of Mg_4Zn_7 [51,52,54]. The growth of the layer with the antiphase against the substrate may occur by nucleation of a mismatched embryo, similar to the growth of an η_2 crystal with stacking faults. However, another mechanism for the formation of the antiphase boundary can be proposed here. Two η_1 particles, which are precipitated on the $(00\bar{1})_{Al}$ planes with a short spacing, develop in layer-by-layer growth, encounter each other, and then coalesce into one particle. When the stacking order of the merged region is different from those of the regular R/R^{-1} stackings, coalescence accompanied by an antiphase grain boundary will occur. In this case, the antiphase grain boundary has a complicated structure wherein the Zn, Cu and Mg atoms near their surfaces are rearranged, leading to the boundary layer being composed of flattened hexagons, as shown in Figs. 5a and b. Subsequently, the particle grows further and the grain boundary has a possibility to be curved. Thus, the precipitate in Fig. 5a can be regarded as the result of coalescence of several η_1 particles. Fig. 5b shows an enlarged image of the area of the yellow frame in Fig. 5a, where an R/R^{-1} rhombohedral unit and a flattened hexagonal unit are illustrated. Supposed positions of Zn and Mg columns in the flattened hexagonal unit are shown for comparison with the Zn and Mg columns in the R/R^{-1} rhombohedral unit. As compared with Fig. 5a, the inverse FFT image in Fig. 5f reveals thinner layers in the Al matrix enclosing the η_1 precipitate. This supports the lateral or layer-by-layer growth of the precipitate by rhomb-unit layers.

Highly complicated defect structures were found in Figs. 5a and b. Supplementary Fig. 4a (Supplementary Material II) displays irregular arrangements, such as a rhombic unit surrounded by several pairs of flattened hexagonal/rhombic units (Supplementary Fig. 4b in Supplementary Material II) and a random flattened hexagonal unit connecting with rhombic units (Supplementary Fig. 4c in Supplementary Material II), which are probably consistent with the varied atomic configurations caused by the effect of the dislocation-assisted precipitate formation in the Zn-Mg alloy [56]. Furthermore, Fig. 5f discloses much more clearly the structure of η_1, comprising the areas constructed with the regular $RR^{-1}RR^{-1}$ layers, the fault layers of flattened-hexagons between them, and other defects. The origin of the complicated structures is unclear but may be assumed to result from the coalescence between precipitates formed on different $\{001\}_{Al}$ habit planes.

The HAADF-STEM image in Fig. 6a shows an η_1 precipitate observed along the $[110]_{Al}$ zone axis. This precipitate has a habit plane along the interface of the $(00\bar{2})_{Al}//(10\bar{1}0)\eta_1$ plane. Particularly, its configuration contains the flattened hexagonal units connected with one or two rhombohedral units distributed along different orientations (i.e., the flattened directions respectively lie on the different planes of $(00\bar{2})_{Al}$ and $(1\bar{1}\bar{1})_{Al}$). Although the differently-oriented flattened hexagonal units are similar to the atomic structure of planar defects within Mg_4Zn_7 reported in previous investigations [52,54], the continuously-connected flattened hexagonal units are completely inconsistent with the typical structure of Mg_4Zn_7 [51,52,54]. They were presumably caused by the introduced defects such as vacancies, dislocations, and stacking faults, or the coalescence of two variants of η_1 during the growth of precipitates. Thus, this characteristic of η_1 (Fig. 6a) should be further investigated by using the stimulated atomic models in the further work. Fig. 6b shows an enlarged image of the area indicated by the frame in Fig. 6a. It explicitly reveals that the structures, composed of a rhombohedron and a flattened-hexagon unit, are similar to those in position b in Fig. 5a.

The atomic structure of the rhombohedron was elucidated by HR-STEM and first principle calculation [3,11,18,19], while the flattened hexagon unit was only observed in the projected atomic-scale micrographs, and its structures were assumed [3,11]. Fig. 6c shows the enlarged images of the areas indicated by the frames in Fig. 6b. The intensity profiles along Line (e) and Line (f) in Fig. 6d, which is the same image as Fig. 6c, are illustrated in Figs. 6e and f, respectively. By taking the Z contrast, the line profiles definitely placed the Mg atomic columns as well as the Zn and Zn/Mg atomic columns in both the rhombohedral unit and the flattened hexagonal unit. The positions of Mg, Zn, and Zn/Mg atomic columns are respectively indicated by blue, red, and orange circles in Fig. 6d.

The various morphologies of all the η types listed in Table 1 are presumably associated with the different growth rates of crystal facets. Regarding their orientation relationships with respect to the Al matrix, the edge-on configurations of plate-like, rod-like or prism-like η are difficult to distinguish with low magnification TEM/STEM. As previously reported [7,43], an effective strategy for extrapolating the morphologies of the hexagonal close-packed precipitates is based on the calculations of lattice misfits in three growth directions with respect to the (0001) basal plane (i.e., one is the lateral growth direction vertical to the basal plane, and the others belong to the layer-by-layer growth direction parallel to the basal plane). The coherency interfaces with the smaller lattice misfit would lower the energy barrier of the precipitate growth. Therefore, the inversely proportional relationship between the lattice misfit and the growth rate can also be employed to evaluate the morphologies of η_1 precipitates.

The misfit vertical to the $(0001)\eta_1$ basal plane ($\delta(v)_{[0001]}$) was relatively smaller: $|d[0001]\eta_1 - 3\,d[1\bar{1}0]_{Al}|/3\,d[1\bar{1}0]_{Al} = |(0.828-0.858)|/0.858 \approx 3.4\%$, whereas the two misfits along the $[10\bar{1}0]\eta_1$ and $[11\bar{2}0]\eta_1$ directions on the $(0001)\eta_1$ basal plane, respectively ($\delta(p)_{[11\bar{2}0]}$ and $\delta(p)_{[10\bar{1}0]}$ for η_1), were relatively large: $\delta(p)_{[11\bar{2}0]} = |d[11\bar{2}0]\eta_1 - d[110]_{Al}|/d[110]_{Al} = |0.252-0.286|/0.286 \approx 11.8\%$, and $\delta(p)_{[10\bar{1}0]} = |d[10\bar{1}0]\eta_1 - d[001]_{Al}|/d(001)_{Al} = |(0.436-0.405)|/0.405 \approx 7.7\%$, where $a = 0.504$ nm and

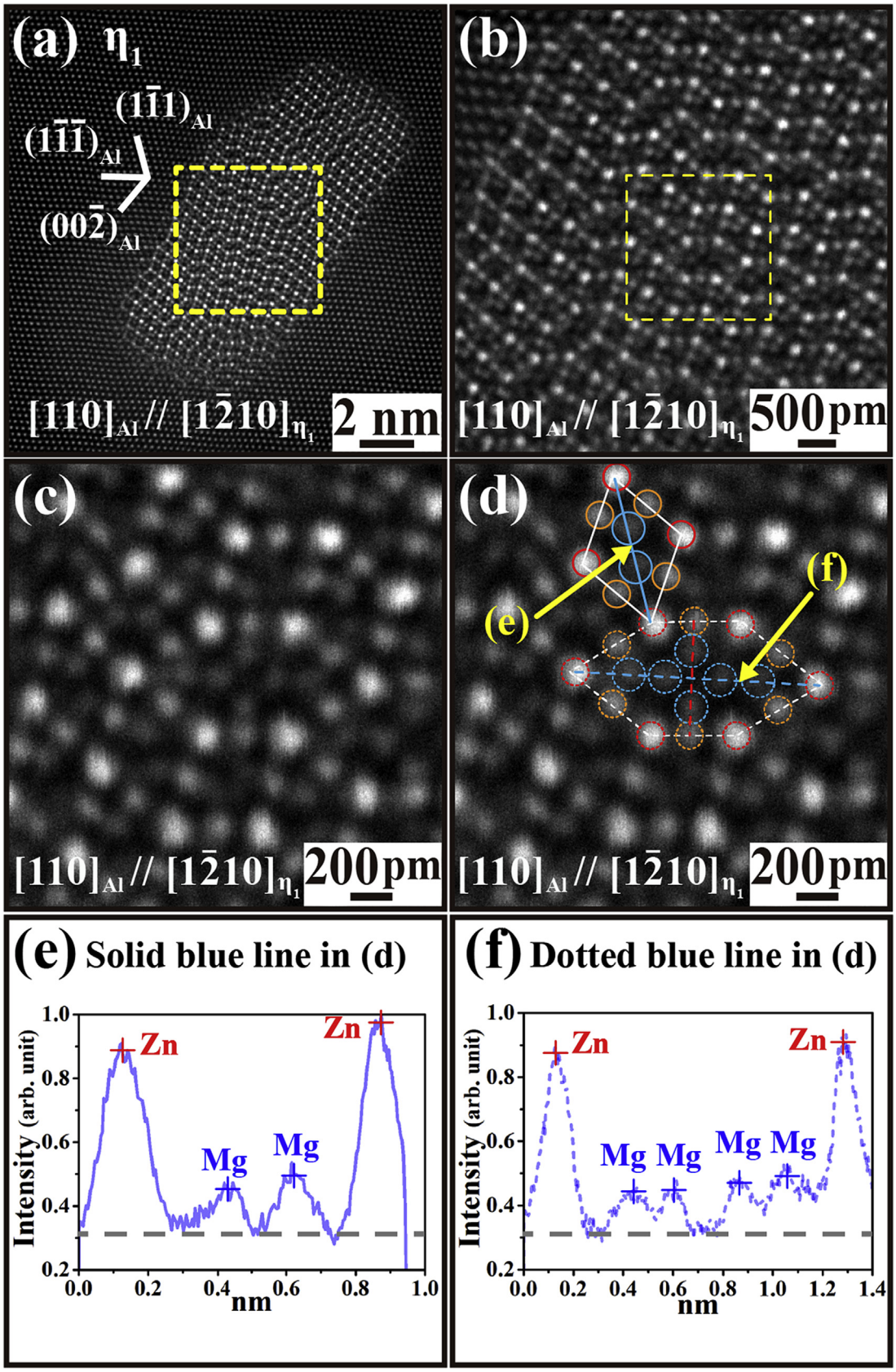

Fig. 6. An η_1 precipitate in the CAF Al alloy. (a) A HAADF-STEM image taken along the $[110]_{Al}//[1\bar{2}10]\eta_1$ zone axis showing its edge-on configuration and the rhombohedron and the flattened hexagonal units. (b) An enlarged image of the area indicated by the frame in (a). (c, d) Enlarged images of the area indicated by the frame in (b), showing a rhombohedral-like unit and a flattened hexagonal structure. Red, orange, and blue circles indicate Zn, Zn/Mg, and Mg atomic columns, respectively. (e) Intensity profile along the line **e** indicated in (d). (f) Intensity profile along the line **f** indicated in (d). (For interpretation of the references to colour in this figure legend, the reader is referred to the Web version of this article.)

c = 0.828 nm for η_1 precipitates [63]. Detailed schematic diagrams indicating the lattice misfits of η_1 precipitates in three growth directions with respect to the Al matrix are provided in Supplementary Fig. 5 (Supplementary Material II). To sum up, the smaller lattice misfits in the $[0001]\eta_1//[1\bar{1}0]_{Al}$ direction would be the preferential growth direction with respect to the $[11\bar{2}0]\eta_1//[110]_{Al}$ and $[10\bar{1}0]\eta_1//[001]_{Al}$ directions. Therefore, it can be confirmed that η_1 would possess the rod-like morphology with the elongated axis along the $[0001]\eta_1//[1\bar{1}0]_{Al}$ direction, instead of the plate-like morphology reported in previous investigations [7,11].

As indicated in Table 1, while previous investigations [7,11,12,45,48] have revealed the slight difference in the orientation relationships between η_1 and η_9 precipitates, few of these studies have looked at the morphology of η_9. The schematic diagrams of the lattice misfit calculations in three growth directions of η_9 (i.e., $\delta(v)_{[0001]}$, $\delta(p)_{[11\bar{2}0]}$, and $\delta(p)_{[10\bar{1}0]}$) are also portrayed in Supplementary Fig. 6 (Supplementary Material II). The misfit vertical to the $(0001)\eta_9$ basal plane, $\delta(v)_{[0001]}$, was $|d[0001]\eta_9 - 3\,d[1\bar{1}0]_{Al}|/3\,d[1\bar{1}0]_{Al} = |0.828-0.858|/0.858 \approx 3.4\%$, and the two misfits along the $[10\bar{1}0]\eta_9$ and $[11\bar{2}0]\eta_9$ directions on the $(0001)\eta_9$ basal plane were $\delta(p)_{[11\bar{2}0]} = |\,3\,d[11\bar{2}0]\eta_9 - 2\,d[001]_{Al}|/2\,d[001]_{Al} = |0.756-0.810|/0.810 \approx 6.7\%$, and $\delta(p)_{[10\bar{1}0]} = |\,2\,d[10\bar{1}0]\eta_9 - 3\,d[110]_{Al}|/3\,d[110]_{Al} = |0.873\text{-}0.858|/0.858 \approx 1.7\%$, where a = 0.504 nm and c = 0.828 nm for η_9 precipitates [63]. For this case, it can be assumed that the higher growth rate in the $[10\bar{1}0]\eta_9$ direction would promote the smaller growth rate in the $[11\bar{2}0]\eta_9$ direction on the $(0001)\eta_9$ basal plane. Therefore, all three growth rates with respect to the $(0001)\eta_9$ basal plane would be nearly equal, thereby resulting in the hexagonal prism morphology of the η_9 precipitate. However, owing to the small volume fraction of η_9 [11,12,16,45], its morphology and atomic structure are difficult to confirm by TEM/STEM micrographs.

Here, a special illustration comparing the atomic structures of η_1 and η_9 is presented in Fig. 7. Cs-corrected HR-STEM images along the $[110]_{Al}$ zone axis show that the edge-on configurations of η_1 and η_9 on the $(00\bar{2})_{Al}$ planes (Figs. 7a and b) possess similar structures, namely, the stacking faults (the yellow arrows in Figs. 7a and b) separating two specific atomic arrays. In Fig. 7a, the edge-on configuration of η_1, the different orientations and the continuous connections of flattened hexagonal arrays are totally distinct from those of the typical Mg_4Zn_7 structures [51,52,54]. In Fig. 7b, the edge-on configuration of η_9 reveals that its central part appears to be composed of the segregated Zn-column layers with the higher Z-contrast, and apart from the centre, it has more closely-packed atomic arrays of Mg and Zn/Mg atomic columns. Between them, blurred stacking faults composed of Mg or vacancies appear to be exist. Furthermore, the higher averaged Z-contrast of η_9 than of η_1 probably implies that the edge-on configuration of η_9 with a hexagonal prism morphology possessed a larger amount of atomic columns (i.e., a higher thickness parallel to the zone axis) than that of η_1 with a rod-like morphology. For more positive identification of η_1 and η_9, the individual FFT diffractograms and simulated patterns were applied, as presented in Figs. 7c and e for η_1, and 7d and 7f for η_9, respectively. The $10\bar{1}0\eta_1$ and $0002\eta_1$ poles were parallel to the 002_{Al} and $2\bar{2}0_{Al}$ poles, respectively, along the $[1\bar{2}10]\eta_1//[110]_{Al}$ zone axis. On the other hand, the $10\bar{1}0\eta_9$ and $0002\eta_9$ poles were parallel to the $2\bar{2}0_{Al}$ and 002_{Al} poles, respectively, along the $[1\bar{1}00]\eta_9//[110]_{Al}$ zone axis.

Fig. 8a shows an HR-HAADF STEM image of an η-precipitate observed along the $[110]_{Al}$ zone axis. It might be the first HR image taken along the $[0001]\eta$ axis and exhibits the hexagonal stacking configuration of a $MgZn_2$ structure. This atomic array is similar to that of Q phases with the hexagonal unit cell, observed along the $[001]_{Al}//[0001]_Q$ zone axis in the Al-Mg-Si-Cu aluminium alloys [77,82]. Fig. 8b shows an enlarged image of the area indicated by the frame in Fig. 8a, and Figs. 8c and d show the FFT diffractogram from Fig. 8a and the simulated ED spot obtained using $MgZn_2$, respectively. The image in Fig. 8a reveals the hexagonal morphology of the precipitate, which exhibits the $\{\bar{1}2\bar{1}0\}$ habit planes. The {0001} planes that are the surfaces of this specimen may also be its habit planes. In addition, this precipitate may be regarded as an η_4-type, for it seems to have the orientation relationship of the precipitate with the Al matrix such that $(0001)\eta_4//(110)_{Al}$ and $[\bar{1}2\bar{1}0]\eta_4//[\bar{1}1\bar{1}]_{Al}$, as indicated in Table 1. As seen in Figs. 8c and d, however, the $20\bar{2}0\eta$ and $0\bar{2}20\eta$ poles are not parallel to the $1\bar{1}1_{Al}$ and $\bar{1}11_{Al}$ poles, respectively, but the $\bar{2}200\eta$ pole is exactly parallel to the $00\bar{2}_{Al}$ pole. This can be recognized in Fig. 8a, where the $(1\bar{1}00)\eta$ facet is parallel to the $(002)_{Al}$ plane (see the red arrows), but the $(20\bar{2}0)\eta$ and $(0\bar{2}20)\eta$ facets are not parallel to the Al lattice fringes on the $(1\bar{1}1)_{Al}$ and $(\bar{1}11)_{Al}$ planes (see the blue arrows). Therefore, the orientation relation of η_4 with the Al matrix has to change into $(0001)\eta//(110)_{Al}$ and $[1\bar{1}00]\eta//[001]_{Al}$, or we have to name it as a new type of precipitate. Since we cannot identify the atomic structure of η_4 reported in previous papers [2,7,11,12,14,16,18,37,45–47], we temporarily call this precipitate η_4'. Hence, the atomic-scale observation of the precipitates along the $[0001]\eta$ axis allows us to determine the exact orientation of the precipitates with regard to the Al matrix, which is important to elucidate their growth mechanism.

In Fig. 8a, a few $(002)_{Al}$ lattices near the $(\bar{2}200)\eta_4$' (and also the $(2\bar{2}00)\eta_4$') facets have much stronger and weaker contrasts (indicated by red arrows), which are respectively ascribed to Zn and Mg atoms that were segregated, migrated, and occupied Al-sites due to the chemical effect mentioned above. The η_4' precipitate develops by nucleation and lateral growth, being provided with these precursors of Zn and Mg. For the growth of edges of the layer, the similar replacement with Zn and Mg atoms was observed and is indicated by blue arrows in Fig. 8a. Thus, the layer-by-layer growth mechanism of the precipitates formed in these Al alloys has been supported by this observation.

Fig. 8e shows an enlarged and processed image of Fig. 8b, which was partially noise filtered, and emphasizes the Z contrast of atomic columns by means of inverse FFT reconstruction, using appropriately selected reflection spots from the FFT diffractogram (Fig. 8c). Fig. 8f shows the $[0001]\eta$ projection of simulated atomic arrangements in the η-$MgZn_2$ crystal obtained by VASP. From the structure of $MgZn_2$ [69], it turns out that the theoretical Z contrast ratio of red marked Zn columns, unmarked Zn columns, and Mg columns in Fig. 8e could be 900 (2 Zn): 450 (Zn): 244 (2 Mg) ≅ 6 : 3 : 1. The observed image can clearly resolve the difference between Zn atom columns and Mg atom columns. The chemical compositions of every atomic column have yet to be analysed.

Basically all of the η-type precipitates have the structure of $MgZn_2$ crystal, which was analyzed by Komura et al. [69]. Previously, Marioara [18] and Bendo et al. [11] indicated its atomic projection along the $[10\bar{1}0]\eta$ and $[11\bar{2}0]\eta$ zone axes in HAADF-STEM images. As mentioned above, eleven types of precipitates, named η_1 to η_{11}, have been reported. In addition, we have identified another type of precipitate and named it η_4', which was observed in the image along the $[0001]\eta$ axis and presented a striking array of atoms. The differences among these 12 types of η precipitates are mainly ascribed to their orientation relationships with regard to the Al matrix, which lead to different morphologies (i.e., the shapes and habit planes), as shown in Table 1 and Fig. 1.

From this point of view, the following precipitate can be regarded as a new type of η precipitate. Figs. 9a and b show HR HADF-STEM images of an η precipitate possessing a zig-zag structure taken

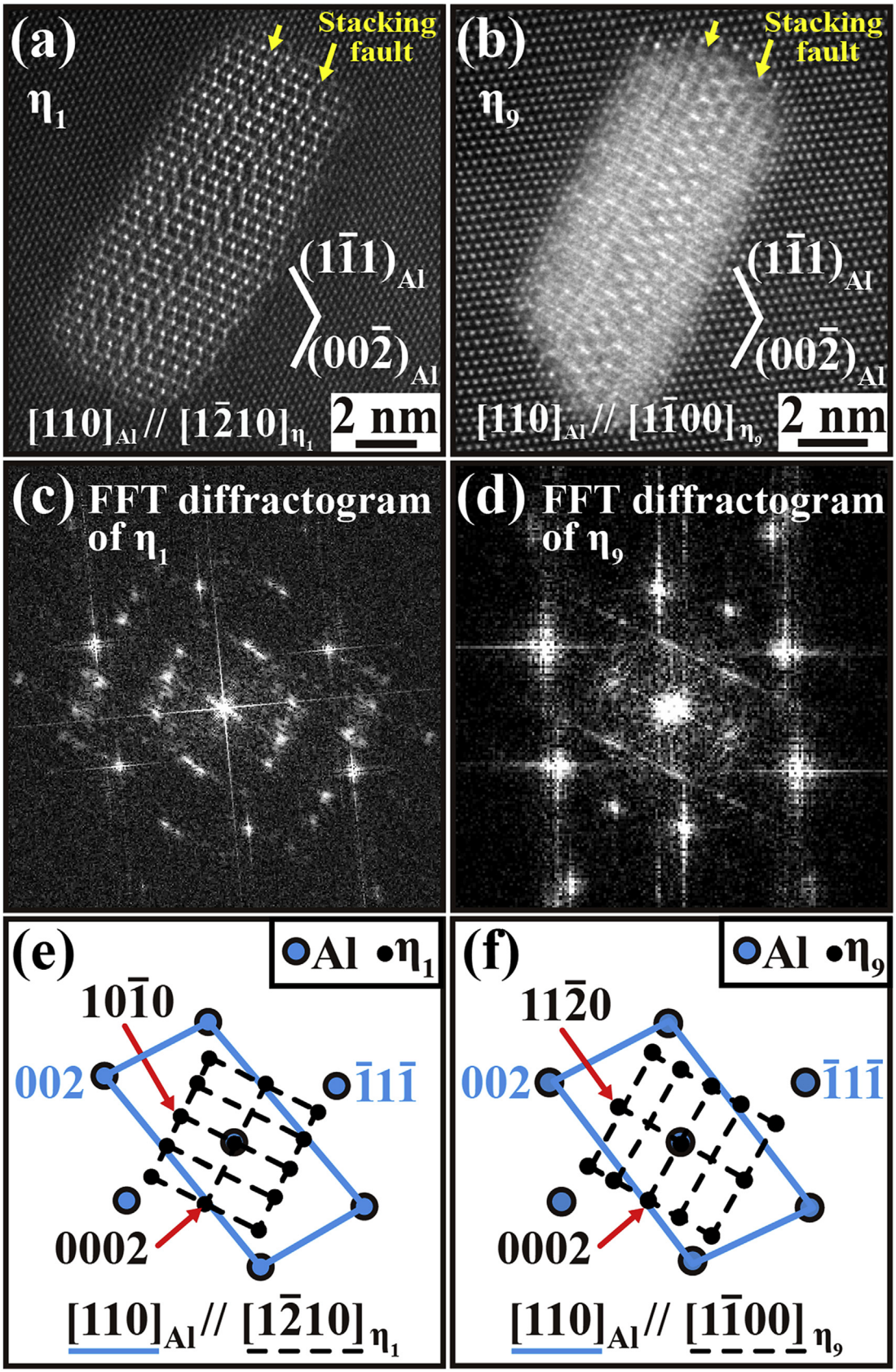

Fig. 7. HR-STEM images along the $[110]_{Al}//[1\bar{2}10]\eta_1//[1\bar{1}00]\eta_9$ zone axis showing (a–b) the edge-on configuration of η_1 and η_9 on the $(00\bar{2})_{Al}$ habit plane, respectively. (c, e) The FFT diffractogram and the simulated diffraction pattern of η_1 with respect to its orientation relationship: $(10\bar{1}0)\eta_1//(001)_{Al}$, $[0001]\eta_1//[1\bar{1}0]_{Al}$, and $[1\bar{2}10]\eta_1//[110]_{Al}$. (d, f) The FFT diffractogram and the simulated diffraction pattern of η_9 with respect to its orientation relationship: $(11\bar{2}0)\eta_9//(001)_{Al}$, $[0001]\eta_9//[1\bar{1}0]_{Al}$, and $[1\bar{1}00]\eta_9//[110]_{Al}$.

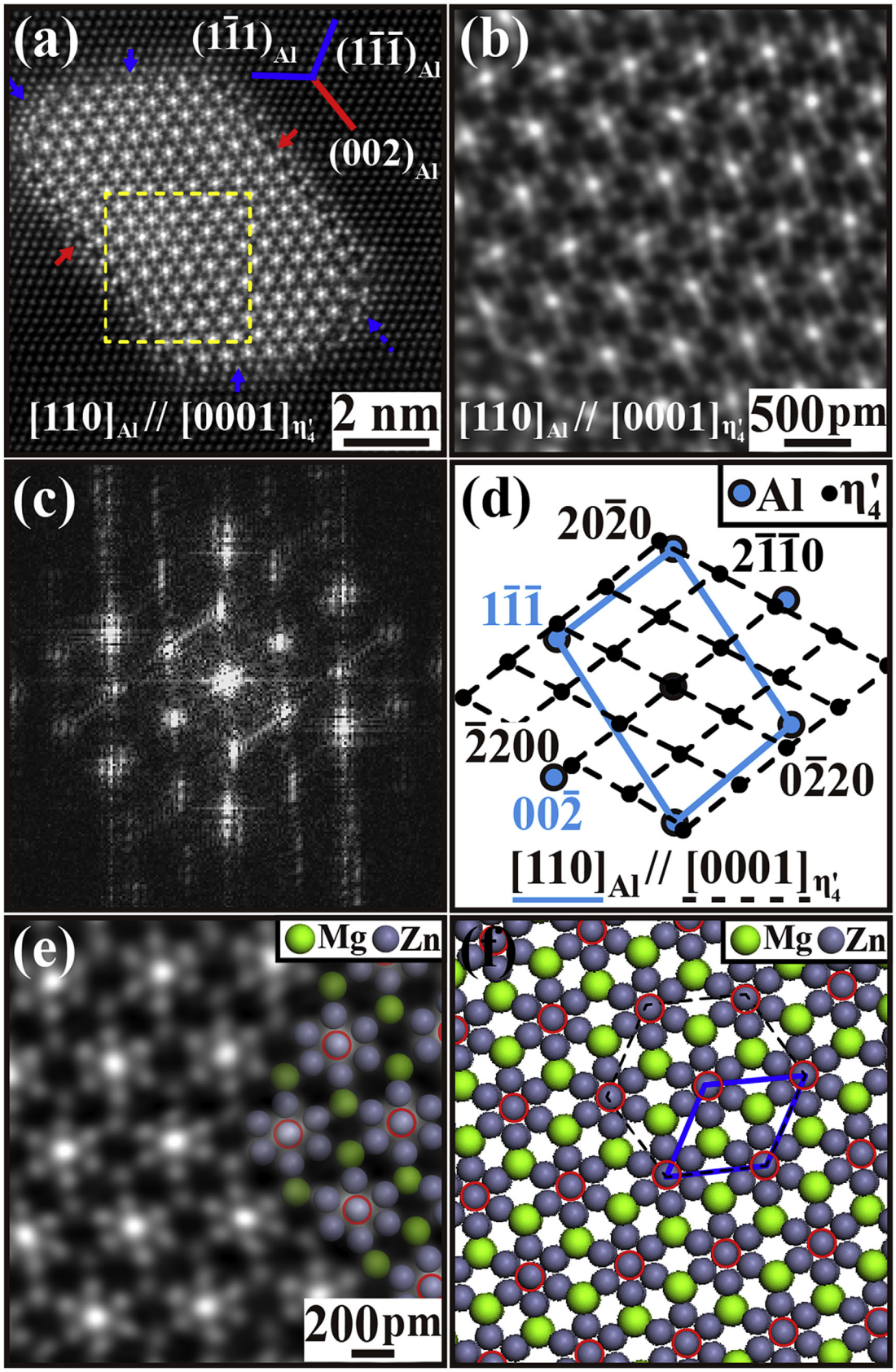

Fig. 8. (a) The (0001) HR-STEM image of an η precipitate in the CAF Al alloy taken along the $[110]_{Al}//[0001]\eta_4'$ zone axis showing its edge-on configuration of the $(2\bar{2}00)\eta$ plane on the $(002)_{Al}$ plane. (b) An enlarged image of the area indicated by the frame in (a). (c) FFT diffractogram from (a). (d) Simulated ED pattern. (e) An enlarged configuration, processed image of part of (a), showing hexagonal stacking together with the structure model. (f) The structure of $MgZn_2$ projected along the $[110]_{Al}//[0001]\eta_4'$ zone axis. The precipitate was named η_4' as it has a new orientation relationship of $(0001)\eta_4'//(110)_{Al}$ and $[1\bar{1}00]\eta_4'//[001]_{Al}$.

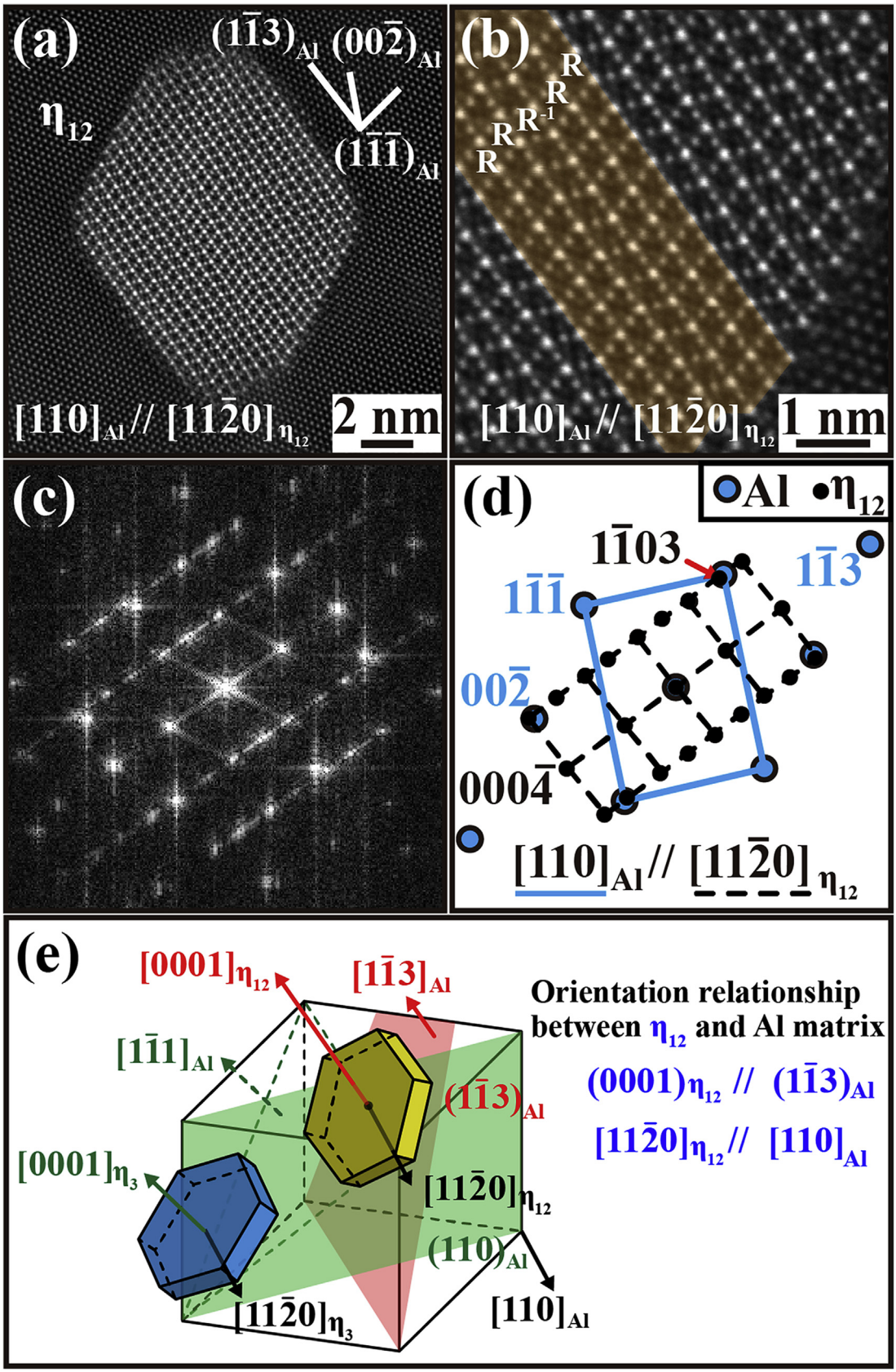

Fig. 9. The new η_{12} precipitate in the CAF Al alloy. (a) A HAADF-STEM image taken along the $[110]_{Al}//[11\bar{2}0]\eta_{12}$ zone axis showing its edge-on configuration of the $(0001)\eta_{12}$ plane on the $(1\bar{1}3)_{Al}$ plane. (b) An enlarged image of (a) showing the disordered rhombohedral stackings (i.e., the five-layer $RRR^{-1}RR$ stackings highlighted in orange) laterally connected with the perfect RR^{-1} stackings. (c) FFT diffractogram of the whole area in (a). (d) Simulated ED pattern for the η_{12} precipitate, indicating a new orientation relationship of $(0001)\eta_{12}//(1\bar{1}3)_{Al}$ and $[11\bar{2}0]\eta_{12}//[110]_{Al}$. (e) Schematic diagram indicating its morphology and the orientation relationship with respect to the Al. For comparison, those for η_3 precipitate are added. (For interpretation of the references to colour in this figure legend, the reader is referred to the Web version of this article.)

along the $[110]_{Al}$ zone axis. From its FFT diffractogram shown in Fig. 9c and the simulated ED pattern illustrated in Fig. 9d, its orientation relationship with the Al matrix was determined to be $(0001)\eta//(1\bar{1}3)_{Al}$ and $[11\bar{2}0]\eta//[110]_{Al}$. Since this orientation relationship has not been reported for any η-type precipitates, we named this new type precipitate η_{12}. It can be regarded as an η_3 precipitate that nucleates on the $(0001)\eta//(1\bar{1}3)_{Al}$ plane instead of on the $(0001)\eta//(1\bar{1}\bar{1})_{Al}$ plane of η_3, keeping the relation of $[11\bar{2}0]\eta_{12}//[11\bar{2}0]\eta_3//[110]_{Al}$, as seen in Fig. 9e. The growth behaviors such as the growth rate of the η_{12} precipitate would be different from that of η_3-type crystal grown on the close-packed $(1\bar{1}\bar{1})_{Al}$ plane. In addition, Fig. 9b shows that the zig-zag R/R^{-1} stacking structure taken along the $[11\bar{2}0]\eta_{12}$ axis, similarly to that of η_2, as shown in Fig. 4. It can be found that in Figs. 9a and b, along the zone axis of $[11\bar{2}0]\eta_{12}$, the disordered rhombohedral stackings, i.e., the five-layer $RRR^{-1}RR$ stackings (highlighted in orange as shown in Fig. 9b), are laterally connected with the perfect RR^{-1} stackings. This stacking faults (i.e., the $RRR^{-1}RR$) would not introduce the formation of flattened hexagonal arrays. This should not be recognized as the same with the characteristic of Mg_4Zn_7 structures [51,52,54].

The structure of Mg_4Zn_7 [51,52,54] supposedly involves with the formation or annihilation of vacancies and dislocations, leading to the change of lattice constants to accommodate the variation of interface energy [44], which would presumably be consistent with the alternations of the stacking sequences in the Laves phases, proposed by Komura et al. [26]. Alternatively, in the present work, vacancies and dislocations can be introduced by the layer-by-layer growth or coalescence of η crystals, changing both the atomic spacing and the electronic state between Zn and Mg solute atoms [21]. The formation of the flattened hexagonal units presumably occurs to reduce the impact of the changes, and under some circumstances these units possibly transform to the perfect rhombohedral units by the annihilation of their intrinsic defect structures. However, this mechanism is still unclear and needs to be confirmed.

4. Conclusions

We have investigated the structures and the growth of η-type precipitates in ageing-treated AA7050 aluminium alloy by means of atomic-scale HAADF-STEM. Conclusively, all η-type precipitates have the approximate structure of $MgZn_2$ crystal, and the differences among the 13 types of η reported so far are ascribed to the orientation relationships with regard to the Al matrix. The important findings from HAADF-STEM observations can be summarized as follows:

1. The η_2-type precipitates observed along the $[10\bar{1}0]\eta_2//[110]_{Al}$ zone axis grew with the $(0001)\eta_2$ habit plane parallel to the $(\bar{1}1\bar{1})_{Al}$ plane. The regular variation of stacking layers along the basal plane (i.e., the sandwiched stacking structure) was confirmed as the projection of each atom column in the η-$ZnMg_2$. The local composition fluctuation was detected in the precipitate as well as in the Al matrix as the difference of Z contrast among the equivalent atomic columns.
2. The η_2-type precipitates observed along the $[1\bar{2}10]\eta_2//[1\bar{1}2]_{Al}$ zone axis grew with the $(0001)\eta_2$ habit plane parallel to the $(1\bar{1}\bar{1})_{Al}$ plane. It was revealed that the regular variation of stacking layers (i.e., the zig-zag stacking structure) was observed to have a sequence of … $RR^{-1}RR^{-1}RR^{-1}$ … along the $(10\bar{1}0)\eta_2$ plane as the projection of the structure of the η-$ZnMg_2$, where R and R^{-1} are different rhombohedral-like units. Stacking faults such as $RR^{-1}R^{-1}R$ or $R^{-1}RRR^{-1}$ were also observed. It was also confirmed in the image of η_1-type precipitates observed along the $[1\bar{2}10]\eta_1//[110]_{Al}$ zone axis that the defect layer composed of flattened hexagons forms as an anti-phase phase boundary between the regular stacking layers. The atomic structures of the R unit and flattened hexagons, in particular the positions of Mg atoms, were determined.
3. Growth steps and strong Z contrast (indicating Z atoms) were observed on the habit plane and in the Al planes near the habit planes, respectively. This suggests that the η precipitates grow layer-by-layer, and this growth is supplied with precursors such as Zn, Cu, or Mg atoms. These solute atoms migrate and become segregated around the interface due to a kind of chemical effect caused by its higher lattice strain energy. The formation of the layer defects is presumably associated with an embryo of the layer growth mismatched in stacking order.
4. Precipitates grown by coalescence of two η_2 particles were observed. The coalescence of crystals precipitated on the same $(1\bar{1}\bar{1})_{Al}$ layers brought about a complicated boundary due to the difference in their stacking orders. The coalescence between crystals precipitated on the $(1\bar{1}1)_{Al}$ and $(1\bar{1}\bar{1})_{Al}$ layers led to a twin-like structure. It was also proposed that the anti-phase boundary in the η_1 can be caused by coalescence of two η_1 particles.
5. The morphologies of η_1 and η_9 precipitates can be estimated by the differences in the lattice misfits in three directions with respect to the $(0001)\eta$ basal plane. For η_1, the smaller lattice misfit vertical to the $(0001)\eta_1$ plane than the two misfits parallel to the $(0001)\eta_1$ plane results in the rod-like shape, and for η_9, the nearly-equal three lattice misfits lead to the hexagonal prism morphology. Furthermore, this is the first report of the atomic configuration of η_9 possessing the sandwiched stacking layers intermitted by stacking faults, similar to the zig-zag atomic configuration embedding the flattened hexagonal faults of η_1.
6. Two new types of η precipitates have been recognized by their orientation relationships with regard to the Al matrix. One is η_4', which can be distinguished from η_4 in the $(0001)\eta_4$ image taken along the $[110]_{Al}$ zone axis and exhibits the atomic configuration (i.e., the hexagonal stacking structure) of $MgZn_2$ along [0001] η_4'. Another is η_{12}, which can be observed with the $(0001)\eta_{12}$ habit plane parallel to the $(1\bar{1}3)_{Al}$ plane in the $[11\bar{2}0]\eta_{12}$ image taken along the $[110]_{Al}$ zone axis.

Acknowledgement

This work was carried out with the financial support from SMART Center of NTU-NIMS and the Ministry of Science and Technology (Taiwan) under Contract MOST106-2923-E-002-009MY2. The authors are grateful to Taiwan Instrument Research Institute and Materials Analysis Technology Inc. (MA-tek) for the technical advice.

Appendix A. Supplementary data

Supplementary data to this article can be found online at https://doi.org/10.1016/j.actamat.2019.05.041.

References

[1] S. Ringer, K. Hono, Microstructural evolution and age hardening in aluminium alloys: atom probe field-ion microscopy and transmission electron microscopy studies, Mater. Char. 44 (2000) 101–131.
[2] J. Gjønnes, C.J. Simensen, An electron microscope investigation of the microstructure in an aluminium-zinc-magnesium alloy, Acta Metall. Mater. 18 (1970) 881–890.
[3] S.J. Andersen, C.D. Marioara, J. Friis, S. Wenner, R. Holmestad, Precipitates in aluminium alloys, Adv. Phys. X 3 (2018) 790–813.
[4] L.K. Berg, J. Gjønnes, V. Hansen, X.Z. Li, M. Knutson-Wedel, G. Waterloo, D. Schryvers, L.R. Wallenberg, GP-zones in Al–Zn–Mg alloys and their role in

artificial aging, Acta Mater. 49 (2001) 3443–3451.
[5] G. Sha, A. Cerezo, Early-stage precipitation in Al–Zn–Mg–Cu alloy (7050), Acta Mater. 52 (2004) 4503–4516.
[6] X.J. Jiang, J. Tafto, B. Noble, B. Holme, G. Waterloo, Differential scanning calorimetry and electron diffraction investigation on low-temperature aging in Al-Zn-Mg alloys, Metall. Mater. Trans. A 31 (2000) 339–348.
[7] T.-F. Chung, Y.-L. Yang, B.-M. Huang, Z. Shi, J. Lin, T. Ohmura, J.-R. Yang, Transmission electron microscopy investigation of separated nucleation and in-situ nucleation in AA7050 aluminium alloy, Acta Mater. 149 (2018) 377–387.
[8] M. Dumont, W. Lefebvre, B. Doisneau-Cottignies, A. Deschamps, Characterisation of the composition and volume fraction of η′ and η precipitates in an Al–Zn–Mg alloy by a combination of atom probe, small-angle X-ray scattering and transmission electron microscopy, Acta Mater. 53 (10) (2005) 2881–2892.
[9] P. Dai, X. Luo, Y. Yang, Z. Kou, B. Huang, C. Wang, J. Zang, J. Ru, Nano-scale precipitate evolution and mechanical properties of 7085 aluminum alloy during thermal exposure, Mater. Sci. Eng. A 729 (2018) 411–422.
[10] W. Yang, S. Ji, M. Wang, Z. Li, Precipitation behaviour of Al–Zn–Mg–Cu alloy and diffraction analysis from η′ precipitates in four variants, J. Alloy. Comp. 610 (2014) 623–629.
[11] A. Bendo, K. Matsuda, S. Lee, K. Nishimura, N. Nunomura, H. Toda, M. Yamaguchi, T. Tsuru, K. Hirayama, K. Shimizu, H. Gao, K. Ebihara, M. Itakura, T. Yoshida, S. Murakami, Atomic scale HAADF-STEM study of η′ and η_1 phases in peak-aged Al–Zn–Mg alloys, J. Mater. Sci. 53 (2018) 4598–4611.
[12] H. Degischer, W. Lacom, A. Zahra, C. Zahra, Decomposition processes in an Al-5%Zn-1%Mg alloy, PartII: Electromicroscopic Invest. Z. Metallk. 71 (1980) 231–238.
[13] D. Godard, P. Archambault, E. Aeby-Gautier, G. Lapasset, Precipitation sequences during quenching of the AA 7010 alloy, Acta Mater. 50 (2002) 2319–2329.
[14] G. Sha, Y.B. Wang, X.Z. Liao, Z.C. Duan, S.P. Ringer, T.G. Langdon, Influence of equal-channel angular pressing on precipitation in an Al–Zn–Mg–Cu alloy, Acta Mater. 57 (2009) 3123–3132.
[15] J.C. Werenskiold, A. Deschamps, Y. Bréchet, Characterization and modeling of precipitation kinetics in an Al–Zn–Mg alloy, Mater. Sci. Eng. A 293 (1–2) (2000) 267–274.
[16] H. Löffler, I. Kovacs, J. Lendvai, Decomposition processes in Al-Zn-Mg alloys, J. Mater. Sci. 18 (1983) 2215–2240.
[17] H. Zhao, F. De Geuser, A. Kwiatkowski da Silva, A. Szczepaniak, B. Gault, D. Ponge, D. Raabe, Segregation assisted grain boundary precipitation in a model Al-Zn-Mg-Cu alloy, Acta Mater. 156 (2018) 318–329.
[18] C.D. Marioara, W. Lefebvre, S.J. Andersen, J. Friis, Atomic structure of hardening precipitates in an Al–Mg–Zn–Cu alloy determined by HAADF-STEM and first-principles calculations: relation to η-$MgZn_2$, J. Mater. Sci. 48 (2013) 3638–3651.
[19] X. Xu, J. Zheng, Z. Li, R. Luo, B. Chen, Precipitation in an Al-Zn-Mg-Cu alloy during isothermal aging: atomic-scale HAADF-STEM investigation, Mater. Sci. Eng. A 691 (2017) 60–70.
[20] M.D. Graef, M.E. McHenry, Metallic Structures Ll: Complex Geometrically Determined Structures, Chapter 18, Structure of Materials: an Introduction to Crystallography, Diffraction and Symmetry, Cambridge University Press, 2012, pp. 466–496.
[21] F. Stein, M. Palm, G. Sauthoff, Structure and stability of Laves phases. Part I. Critical assessment of factors controlling Laves phase stability, Intermetallics 12 (2004) 713–720.
[22] Y. Komura, Stacking faults and two new modifications of the Laves phase in Mg–Cu–Al system, Acta Crystallogr. 15 (1962) 770–778.
[23] Y. Komura, Y. Kitano, Long-period stacking variants and their electron-concentration dependence in the Mg-base Friauf–Laves phases, Acta Crystallogr. B 33 (1977) 2496–2501.
[24] P.M. Hazzledine, P. Pirouz, Synchroshear transformations in Laves phases, Scripta Metall. Mater. 28 (1993) 1277–1282.
[25] Y. Kitano, Y. Komura, H. Kajiwara, E. Watanabe, Two-dimensional lattice image of the Mg-base Friauf–Laves phase and a new type of defect, Acta Crystallogr. - Sect. A Cryst. Phys. Diffr. Theor. Gen. Crystallogr. 36 (1980) 16–21.
[26] Y. Komura, E. Kishida, M. Inoue, The crystal structure of the Laves phase in Mg-Zn-Ag-system. I, J. Phys. Soc. Jpn. 23 (1967) 398–404.
[27] K.S. Kumar, P.M. Hazzledine, Polytypic transformations in Laves phases, Intermetallics 12 (2004) 763–770.
[28] W.J. Kim, S.I. Hong, K.H. Lee, Structural characterization of Laves-phase $MgZn_2$ precipitated in Mg-Zn-Y alloy, Met. Mater. Int. 16 (2010) 171–174.
[29] M.J. Buerger, Application of Point-Group Symmetries to Crystals, Chapter 7, Introduction to Crystal Geometry, McGraw-Hill, New York, 1971, pp. 52–77.
[30] M.D. Graef, M.E. McHenry, Lattice Planes, Chapter 5, Structure of Materials: an Introduction to Crystallography, Diffraction and Symmetry, Cambridge University Press, 2012, pp. 90–102.
[31] J. Cahn, G. Kalonji, Symmetry in solid state transformation morphologies, in: Proceedings of an International Conference on Solidsolid Phase Transformations, The Metallurgical Society of AIME, Warrendale (PA), 1982, pp. 3–14.
[32] M. Boudeulle, Disproportionation in mineral solid solutions: symmetry constraints on precipitate orientation and morphology. Implications for the study of oriented intergrowths, J. Appl. Crystallogr. 27 (1994) 567–573.
[33] G. Van Tendeloo, S. Amelinckx, Group-theoretical considerations concerning domain formation in ordered alloys, Acta Crystallogr. - Sect. A Cryst. Phys. Diffr. Theor. Gen. Crystallogr. 30 (1974) 431–440.
[34] A. Redjaimia, P. Ruterana, G. Metauer, M. Gantois, Identification and characterization of a novel intermetallic compound in a Fe-22 wt% Cr-5 wt% Ni-3 wt % Mo-0.03 wt% C duplex stainless steel, Philos. Mag. A 67 (5) (1993) 1277–1286.
[35] C.Q. Liu, H.W. Chen, H. Liu, X.J. Zhao, J.F. Nie, Metastable precipitate phases in Mg–9.8 wt%Sn alloy, Acta Mater. 144 (2018) 590–600.
[36] H. Liu, B. Bellón, J. Llorca, Multiscale modelling of the morphology and spatial distribution of θ′ precipitates in Al-Cu alloys, Acta Mater. 132 (2017) 611–626.
[37] X.Z. Li, V. Hansen, J. GjØnnes, L.R. Wallenberg, HREM study and structure modeling of the η′ phase, the hardening precipitates in commercial Al–Zn–Mg alloys, Acta Mater. 47 (1999) 2651–2659.
[38] O. Skiba, A. Redjaïmia, J. Dulcy, J. Ghanbaja, G. Marcos, N. Caldeira-Meulnotte, T. Czerwiec, A proper assessment of TEM diffraction patterns originating from CrN nitrides in a ferritic matrix, Mater. Char. 144 (2018) 671–677.
[39] C. Cayron, Groupoid of orientational variants, Acta Crystallogr. A: Found. Crystallogr. 62 (2006) 21–40.
[40] G. Thorkildsen, H.B. Larsen, Crystallography of embedded particles in Al-Mg-Zn alloys. Symmetry analysis, J. Appl. Crystallogr. 47 (2014) 1736–1748.
[41] A.R.S. Gautam, J.M. Howe, A method to predict the orientation relationship, interface planes and morphology between a crystalline precipitate and matrix: part II–application, Phil. Mag. 93 (2013) 3472–3490.
[42] A.R.S. Gautam, J.M. Howe, A method to predict the orientation relationship, interface planes and morphology between a crystalline precipitate and matrix. Part I. Approach, Phil. Mag. 91 (2011) 3203–3227.
[43] T.-F. Chung, Y.-L. Yang, C.-N. Hsiao, W.-C. Li, B.-M. Huang, C.-S. Tsao, Z. Shi, J. Lin, P.E. Fischione, T. Ohmura, J.-R. Yang, Morphological evolution of GP zones and nanometer-sized precipitates in the AA2050 aluminium alloy, Int. J. Lightweight Mater. Manuf. 1 (2018) 142–156.
[44] J. Sun, L. Fu, H. Liu, S.P. Ringer, Z. Liu, Interpretation of the vacancy-ordering controlled growth morphology of $Hg_5In_2Te_8$ precipitates in $Hg_3In_2Te_6$ single crystals by TEM observation and crystallographic calculation, J. Alloy. Comp. 622 (2015) 206–212.
[45] P. Auger, J. Raynal, M. Bernole, R. Graf, X-ray and electron-microscopy study of precipitation in Al-Zn-Mg and Al-Zn-Mg-Cu alloys tempered between 100 and 300 C, Mem. Sci. Rev. Met. 71 (1974) 557–568.
[46] P.A. Tracery, The nature and morphology of precipitate in Al-Zn-Mg alloys, J. Inst. Met. 96 (1968) 228–235.
[47] H. Schmalzried, V. Gerold, Age-hardening in an Al-Mg-Zn alloy, Z. Metallk. 49 (1958) 291–301.
[48] J.D. Embury, R.B. Nicholson, The nucleation of precipitates: the system Al-Zn-Mg, Acta Metall. Mater. 13 (1965) 403–417.
[49] J. Park, A. Ardell, Microstructures of the commercial 7075 Al alloy in the T651 and T7 tempers, Metall. Trans. A 14 (1983) 1957–1965.
[50] A. Singh, J.M. Rosalie, H. Somekawa, T. Mukai, The structure of precipitates in Mg–Zn–Y alloys, Phil. Mag. Lett. 90 (2010) 641–651.
[51] A. Singh, Tailoring microstructure of Mg–Zn–Y alloys with quasicrystal and related phases for high mechanical strength, Sci. Technol. Adv. Mater. 15 (2014) p1–p16, 044803.
[52] A. Singh, J.M. Rosalie, Lattice correspondence and growth structures of monoclinic Mg_4Zn_7 phase growing on an icosahedral quasicrystal, Crystals 8 (2018) 194.
[53] A. Singh, A.P. Tsai, Structural characteristics of β'_1 precipitates in Mg–Zn-based alloys, Scripta Mater. 57 (2007) 941–944.
[54] J.M. Rosalie, H. Somekawa, A. Singh, T. Mukai, Structural relationships among $MgZn_2$ and Mg_4Zn_7 phases and transition structures in Mg-Zn-Y alloys, Phil. Mag. 90 (2010) 3355–3374.
[55] J.M. Rosalie, H. Somekawa, A. Singh, T. Mukai, Orientation relationships between icosahedral clusters in hexagonal $MgZn_2$ and monoclinic Mg_4Zn_7 phases in Mg-Zn(-Y) alloys, Phil. Mag. 91 (2011) 2634–2644.
[56] Z. Yang, L. Zhang, M.F. Chisholm, X. Zhou, H. Ye, S.J. Pennycook, Precipitation of binary quasicrystals along dislocations, Nat. Commun. 9 (2018) 809–816.
[57] H. Jiao, C. Li, The HREM study of precipitates in an Al– Zn– Mg alloy, Adv. Perform. Mater. 2 (1995) 305–309.
[58] Y.-L. Yang, A.C. Lam, Z. Shi, J. Lin, R. Said, Constitutive Modelling of Creep-Ageing Behaviour of Peak-Aged Aluminium Alloy 7050, Matec. Web. Conf., EDP Sciences, 2015.
[59] K. Watanabe, T. Yamazaki, Y. Kikuchi, Y. Kotaka, M. Kawasaki, I. Hashimoto, M. Shiojiri, Atomic-resolution incoherent high-angle annular dark field STEM images of Si(011), Phys. Rev. B 63 (2001) 085316.
[60] K. Watanabe, N. Nakanishi, T. Yamazaki, M. Kawasaki, I. Hashimoto, M. Shiojiri, Effect of incident probe on HAADF STEM images, Phys. Status Solidi 235 (2003) 179–188.
[61] G. Kresse, J. Furthmüller, Efficient iterative schemes for ab initio total-energy calculations using a plane-wave basis set, Phys. Rev. B 54 (1996) 11169–11186.
[62] G. Kresse, D. Joubert, From ultrasoft pseudopotentials to the projector augmented-wave method, Phys. Rev. B 59 (1999) 1758–1775.
[63] C. Wolverton, Crystal structure and stability of complex precipitate phases in Al–Cu–Mg–(Si) and Al–Zn–Mg alloys, Acta Mater. 49 (2001) 3129–3142.
[64] T. Yamazaki, M. Kawasaki, K. Watanabe, I. Hashimoto, M. Shiojiri, Effect of small crystal tilt on atomic-resolution high-angle annular dark field STEM imaging, Ultramicroscopy 92 (2002) 181–189.
[65] R. Erni, Scanning Transmission Electron Microscopy, Chapter 3, Aberration-

Corrected Imaging in Transmission Electron Microscopy: an Introduction, World Scientific, 2010.
[66] S.J. Pennycook, P.D. Nellist, Z-contrast Scanning Transmission Electron Microscopy, Chapter 7, Impact of Electron and Scanning Probe Microscopy on Materials Research, Springer Science & Business Media, 1999, pp. 161–207.
[67] M. Shiojiri, H. Saijo, Imaging of high-angle annular dark-field scanning transmission electron microscopy and observations of GaN-based violet laser diodes, J. Microsc. 223 (2006) 172–178.
[68] M. Kawasaki, T. Yamazaki, S. Sato, K. Watanabe, M. Shiojiri, Atomic-scale quantitative elemental analysis of boundary layers in a $SrTiO_3$ ceramic condenser by high-angle annular dark-field electron microscopy, Philos. Mag. A 81 (2001) 245–260.
[69] Y. Komura, K. Tokunaga, Structural studies of stacking variants in Mg-base Friauf–Laves phases, Acta Crystallogr. Sect. B Struct. Crystallogr. Cryst. Chem. 36 (1980) 1548–1554.
[70] Y.-Y. Li, L. Kovarik, P.J. Phillips, Y.-F. Hsu, W.-H. Wang, M.J. Mills, High-resolution characterization of the precipitation behavior of an Al–Zn–Mg–Cu alloy, Phil. Mag. Lett. 92 (2012) 166–178.
[71] H. Suzuki, Chemical interaction of solute atoms with dislocations, Science reports of the Research Institutes, Tohoku University, Ser. A, Phys. Chem. Metall. 4 (1952) 455–463.
[72] D. Rossouw, B. Langelier, A. Scullion, M. Danaie, G.A. Botton, Multivariate-aided mapping of rare-earth partitioning in a wrought magnesium alloy, Scripta Mater. 124 (2016) 174–178.
[73] C. Liu, H. Chen, J.-F. Nie, Interphase boundary segregation of Zn in Mg-Sn-Zn alloys, Scripta Mater. 123 (2016) 5–8.
[74] C.Q. Liu, H.W. Chen, N.C. Wilson, J.F. Nie, Zn segregation in interface between Mg17Al12 precipitate and Mg matrix in Mg–Al–Zn alloys, Scripta Mater. 163 (2019) 91–95.
[75] K. Matsuda, D. Teguri, Y. Uetani, T. Sato, S. Ikeno, Cu-segregation at the Q′/α-Al interface in Al–Mg–Si–Cu alloy, Scripta Mater. 47 (2002) 833–837.
[76] J.M. Rosalie, L. Bourgeois, Silver segregation to θ′ (Al2Cu)–Al interfaces in Al–Cu–Ag alloys, Acta Mater. 60 (2012) 6033–6041.
[77] M. Fiawoo, X. Gao, L. Bourgeois, N. Parson, X.Q. Zhang, M. Couper, J.F. Nie, Formation of multiple orientation relationships of Q precipitates in Al–Mg–Si–Cu alloys, Scripta Mater. 88 (2014) 53–56.
[78] S.J. Kang, Y.-W. Kim, M. Kim, J.-M. Zuo, Determination of interfacial atomic structure, misfits and energetics of Ω phase in Al–Cu–Mg–Ag alloy, Acta Mater. 81 (2014) 501–511.
[79] D. Shin, A. Shyam, S. Lee, Y. Yamamoto, J.A. Haynes, Solute segregation at the Al/θ′-Al2Cu interface in Al-Cu alloys, Acta Mater. 141 (2017) 327–340.
[80] Y. Weng, Z. Jia, L. Ding, K. Du, H. Duan, Q. Liu, X. Wu, Special segregation of Cu on the habit plane of lath-like β′ and QP2 precipitates in Al-Mg-Si-Cu alloys, Scripta Mater. 151 (2018) 33–37.
[81] H.-Y. Shih, M. Shiojiri, C.-H. Chen, S.-F. Yu, C.-T. Ko, J.-R. Yang, R.-M. Lin, M.-J. Chen, Ultralow threading dislocation density in GaN epilayer on near-strain-free GaN compliant buffer layer and its applications in hetero-epitaxial LEDs, Sci. Rep. 5 (2015) 13671.
[82] L. Ding, Z. Jia, J.-F. Nie, Y. Weng, L. Cao, H. Chen, X. Wu, Q. Liu, The structural and compositional evolution of precipitates in Al-Mg-Si-Cu alloy, Acta Mater. 145 (2018) 437–450.